Genetically Defined Syngeneic Mouse Models of Ovarian Cancer as Tools for the Discovery of Combination Immunotherapy

Sonia Iyer[1], Shuang Zhang[2], Simge Yucel[1], Heiko Horn[3,4], Sean G. Smith[5], Ferenc Reinhardt[1], Esmee Hoefsmit[1], Bimarzhan Assatova[1], Julia Casado[6], Marie-Charlotte Meinsohn[4], M. Inmaculada Barrasa[1], George W. Bell[1], Fernando Pérez-Villatoro[6], Kaisa Huhtinen[7], Johanna Hynninen[8], Jaana Oikkonen[6], Pamoda M. Galhenage[9], Shailja Pathania[9], Paula T. Hammond[5], Benjamin G. Neel[2], Anniina Farkkila[6,10], David Pépin[4], and Robert A. Weinberg[1,11,12]

ABSTRACT

Despite advances in immuno-oncology, the relationship between tumor genotypes and response to immunotherapy remains poorly understood, particularly in high-grade serous tubo-ovarian carcinomas (HGSC). We developed a series of mouse models that carry genotypes of human HGSCs and grow in syngeneic immunocompetent hosts to address this gap. We transformed murine-fallopian tube epithelial cells to phenocopy homologous recombination–deficient tumors through a combined loss of *Trp53, Brca1, Pten,* and *Nf1* and overexpression of *Myc* and *Trp53*^{R172H}, which was contrasted with an identical model carrying wild-type *Brca1*. For homologous recombination–proficient tumors, we constructed genotypes combining loss of *Trp53* and overexpression of *Ccne1, Akt2,* and *Trp53*^{R172H}, and driven by *KRAS*^{G12V} or *Brd4* or *Smarca4* overexpression. These lines form tumors recapitulating human disease, including genotype-driven responses to treatment, and enabled us to identify follistatin as a driver of resistance to checkpoint inhibitors. These data provide proof of concept that our models can identify new immunotherapy targets in HGSC.

SIGNIFICANCE: We engineered a panel of murine fallopian tube epithelial cells bearing mutations typical of HGSC and capable of forming tumors in syngeneic immunocompetent hosts. These models recapitulate tumor microenvironments and drug responses characteristic of human disease. In a *Ccne1*-overexpressing model, immune-checkpoint resistance was driven by follistatin.

[1]Whitehead Institute for Biomedical Research, Cambridge, Massachusetts. [2]Laura and Isaac Perlmutter Cancer Center, NYU-Langone Medical Center, New York, New York. [3]Stanley Center, Broad Institute of MIT and Harvard, Cambridge, Massachusetts. [4]Pediatric Surgical Research Laboratories, Massachusetts General Hospital; Department of Surgery, Harvard Medical School, Boston, Massachusetts. [5]Marble Center for Cancer Nanomedicine, Koch Institute for Integrative Cancer Research, Massachusetts Institute of Technology, Cambridge, Massachusetts. [6]Research Program in Systems Oncology, University of Helsinki and Helsinki University Hospital, Helsinki, Finland. [7]Institute of Biomedicine and FICAN West Cancer Centre, University of Turku, Turku, Finland. [8]Department of Obstetrics and Gynecology, University of Turku and Turku University Hospital, Turku, Finland. [9]Center for Personalized Cancer Therapy, University of Massachusetts, Boston, Massachusetts. [10]Dana-Farber Cancer Institute Harvard Medical School, Boston, Massachusetts. [11]Department of Biology, Massachusetts Institute of Technology, Cambridge, Massachusetts. [12]Massachusetts Institute of Technology Ludwig Center for Molecular Oncology, Cambridge, Massachusetts.

Note: Supplementary data for this article are available at Cancer Discovery Online (http://cancerdiscovery.aacrjournals.org/).

Current address for S. Iyer: Translational Medicine, Oncology R&D, AstraZeneca, Boston, Massachusetts.

Corresponding Authors: Robert A. Weinberg, Whitehead Institute for Biomedical Research, 455 Main Street, WHTH-367, Cambridge, MA 02142. Phone: 617-258-5159; Fax: 617-258-5213; E-mail: weinberg@wi.mit.edu; and David Pépin, Pediatric Surgical Research Laboratories, Massachusetts General Hospital; Department of Surgery, Harvard Medical School, Boston, MA 02114. Phone: 617-643-3040; Fax: 617-726-5057; E-mail: DPEPIN@mgh.harvard.edu

Cancer Discov 2021;11:384–407

doi: 10.1158/2159-8290.CD-20-0818

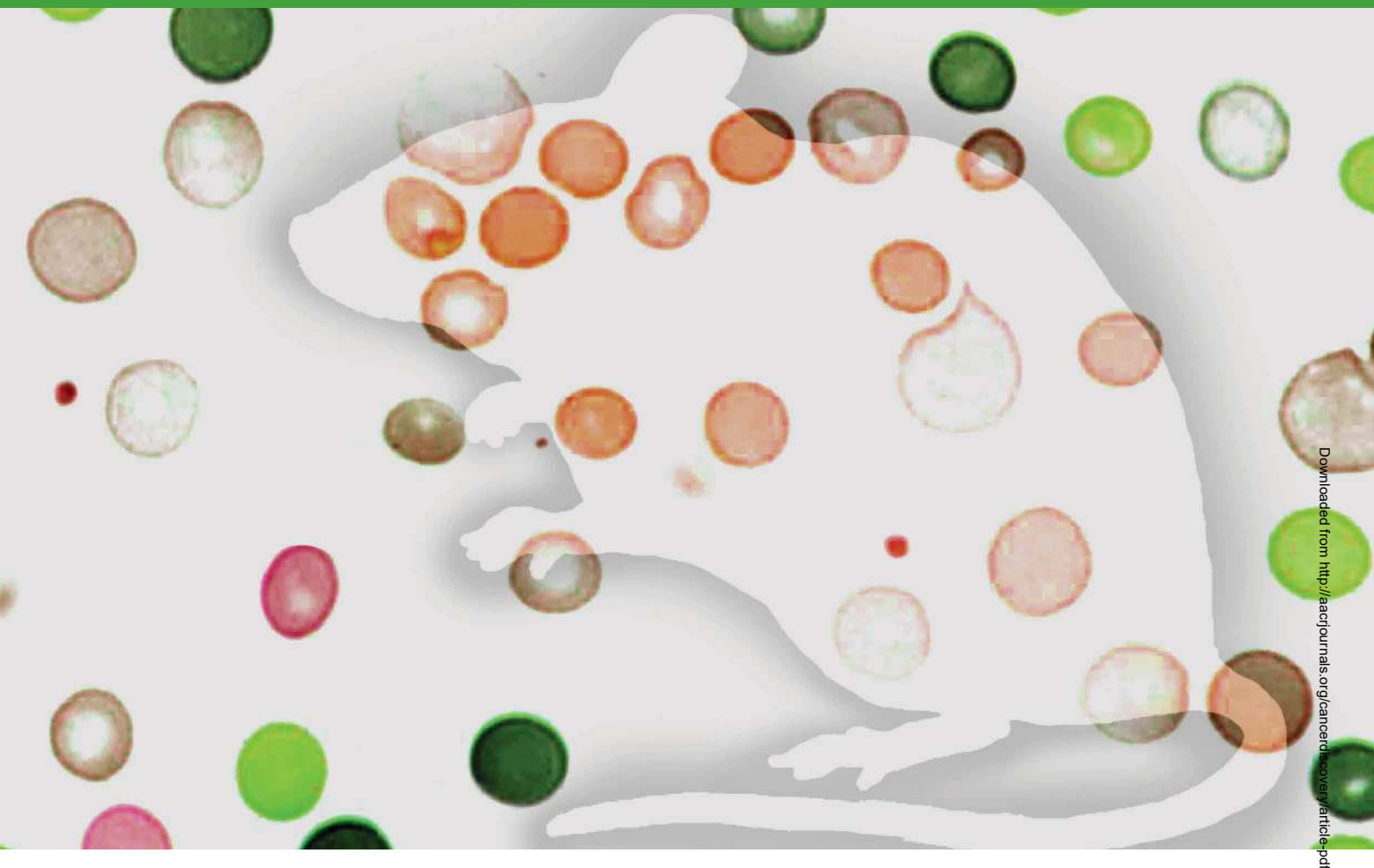

INTRODUCTION

High-grade serous tubo-ovarian carcinomas (HGSC) are characterized by significant structural genomic changes and an almost universally mutated *TP53* gene (1). More than 50% of HGSCs have defects in the homologous recombination (HR)–dependent repair pathway primarily associated with genetic and epigenetic alterations of HR pathway genes, such as *BRCA1, BRCA2*, and *PTEN*. HGSCs with defective HR initially respond well to platinum-based chemotherapy and PARP inhibitors (2). A second, distinct subgroup of ovarian tumors involves approximately 20% of the clinically encountered HGSCs. These tumors exhibit *CCNE1* gene amplification and an intact HR pathway (3) and are associated with a worse response to platinum-based chemotherapy and inferior clinical outcomes (3, 4). This explains why there is an urgent need to develop new therapeutic interventions to treat the various HGSC tumor subtypes, particularly the HR-proficient subgroups.

Immuno-oncology approaches that reverse the immune-suppressive microenvironments of tumors have successfully unleashed the immune system against several tumor types. Still, their successes have been limited in the case of HGSCs (5, 6). Thus, recent clinical data regarding the efficacy of single-agent immune-checkpoint blockade (ICB) therapies indicate limited benefit in recurrent ovarian cancer (7, 8) compared with other tumor types. Precisely why this is the case remains poorly understood, highlighting the need to study the underlying biology of immune evasion in ovarian cancer using immunocompetent animal models. Unfortunately, the preclinical models required to address questions regarding specific HGSC genotypes' contribution to immune evasion have been limited until now. Moreover, because the responses to ICB vary by genotype (9), models that recapitulate the various genomic profiles observed in HGSC are needed.

Currently used models to study HGSC include patient-derived xenografts growing in immunodeficient hosts, limiting the study of tumor–immune interactions (10). In contrast, syngeneic models, such as the commonly used ID8 murine model (11), together with genetically modified versions of these cells (12, 13), have been extensively used to investigate the roles of the immune system in HGSC progression and to study therapeutic responses. Nonetheless, the ID8 model does not carry the common mutations and somatic copy-number alterations observed in human HGSCs (12). Over the years, several genetically engineered transgenic mouse models (GEMM; refs. 14–17) have been developed, including those derived from fallopian tube epithelial (FTE) cells—the presumed normal cells of origin of HGSCs (17–19); although useful, complex combination genotypes are laborious to construct via

crosses between germline mutation–bearing mouse strains. Moreover, such models lack the flexibility to control the timing of tumor outgrowth, rendering them less suitable as preclinical models.

Herein, we generated genetically distinct HGSC cell line models bearing genetic alterations representing human tumors and that can be propagated in fully immunocompetent, syngeneic mouse hosts. We selected the most common combinations of co-occurring mutations observed in the HR-deficient (HRD) spectrum and the HR-proficient (HRP) spectrum HGSC patient samples from The Cancer Genome Atlas (TCGA). We introduced them into *Trp53*$^{-/-}$ or *Trp53*$^{-/-}$*Brca1*$^{-/-}$ mutant (20) FTE cells of C57BL/6 mice using the CRISPR/Cas9 methodology to introduce biallelic deletions and/or lentiviral or retroviral gene transduction to model overexpression. These proof-of-concept preclinical models allowed us to characterize certain mutational spectra's influence on the tumor-immune microenvironment and test new combinations of standard therapies and immunotherapies. Given the unrealized potential of ICB and resistance to current therapies in HGSC, models such as these could reveal novel treatment strategies and identify therapeutic targets to improve women's response rates under treatment.

RESULTS

Generating and Validating the Engineered Murine FTE–Derived Cells with Clinically Relevant Driver Mutations

To produce transformed murine fallopian tube epithelial (m-FTE) cells bearing patient-relevant mutant genotypes, we identified the most common combinations of mutations observed in HR-deficient spectrum and HR-proficient spectrum HGSC patient samples listed in the TCGA data set (Supplementary Fig. S1A). The generation of HR-deficient spectrum genotypes is shown in Fig. 1A. The BPPNM (*Trp53*$^{-/-R172H}$*Brca1*$^{-/-}$*Pten*$^{-/-}$*Nf1*$^{-/-}$*Myc*^{OE} genotype) is HR deficient, and the PPNM (*Trp53*$^{-/-R172H}$*Pten*$^{-/-}$*Nf1*$^{-/-}$*Myc*^{OE} genotype) cell line which does not correspond precisely with a known HR-deficient human HGSC genotype is therefore deemed "nonclassified" (Fig. 1A). For the HR-proficient cell lines, we overexpressed combinations of *CCNE1, AKT2, BRD4*, and *SMARCA4* genes, as well as *KRAS*; these mutant alleles are observed clinically in HGSC tumors with frequencies of 19%, 6%, 12%, 10%, and 12%, respectively (Supplementary Fig. S1A). Derivation of the HR-proficient genotypes is shown in Fig. 1B. Of note, *KRAS*^{G12V}-activating mutation was introduced in the cells to model overexpression (21).

We confirmed the introduced genetic alterations at both the gene and protein levels. Genomic assays were used that were appropriate to the mutant allele being analyzed. *Brca1*$^{-/-}$ (Supplementary Fig. S1B), *Trp53*^{R172H} mutation (Supplementary Fig. S1C), and *KRAS*^{G12V} mutation (Supplementary Fig. S1D) were confirmed using PCR-based analyses. CRISPR-mediated deletion of *Pten* and *Nf1* in the BPPNM and PPNM cell lines was confirmed using the Surveyor assay (ref. 22; Supplementary Fig. S1E). Protein expression was confirmed using Western blot analyses compared with known HGSC cell lines harboring similar mutations (Supplementary Fig. S1F and S1G).

To validate the functionality of the mutations that we had introduced into the engineered m-FTE cells, we performed Western blot analyses of the downstream signaling phosphoprotein targets. In the BPPNM and PPNM cells, loss of *Pten* and *Nf1* genes led to increased AKT, mTOR, and ERK1/2 activation (Supplementary Fig. S1H). m-FTE cells harboring the *Trp53* mutation failed to induce p21 expression upon nocodazole treatment in contrast to corresponding *Trp53* wild-type cells (Supplementary Fig. S1I). Additionally, to test the functionality of the KPCA *KRAS*^{G12V}-overexpressing cell line, we gauged the drug sensitivity *in vitro* to the EGFR inhibitor erlotinib (ref. 23; Supplementary Fig. S1J). To summarize these results, validation of downstream target activation confirmed mutant *KRAS* and *Trp53* allele expression, and the loss of functional *Pten* and *Nf1* genes led to anticipated changes in biochemical and biological responses.

We also used immunofluorescence (Fig. 1C) to verify the continued expression in all of the cell lines of the key FTE markers PAX8 and CK7 (17–19). To determine the HR DNA damage repair efficiency, we tested RAD51 nuclear focus formation in response to ionizing radiation (IR; Fig. 1D). As anticipated, the HR-deficient BPPNM cell line and the nonclassified PPNM cells showed fewer RAD51 nuclear foci relative to HR-proficient cells (Fig. 1D).

We further explored allelic imbalance profiles to assess genomic scarring associated with HR deficiency using shallow whole-genome sequencing (WGS) in the engineered m-FTE cells. Loss of heterozygosity (LOH) is an allelic imbalance signature specific for HR deficiency due to uniparental disomy due to inaccurate repair of sister chromatids during the S–G_2 phase of the cell cycle in HR-deficient cells (24–26). Consistently, the BPPNM cells exhibited the highest LOH events among the engineered m-FTE cells (Supplementary Fig. S2A and S2B). Of additional interest, the SPCA cells had the highest number of LOH events among the HR-proficient mutation-harboring cell lines. These findings confirm the predicted HR DNA-repair capacities of the engineered m-FTE cells.

Engineered m-FTE Cells Exhibit Expected Drug Sensitivities *In Vitro*

We proceeded to evaluate the *in vitro* drug sensitivities of the HR-deficient BPPNM and the PPNM cell lines and the HR-proficient BPCA, SPCA, and KPCA cell lines. As predicted by their respective genotypes, the *Brca1*-deficient cell line BPPNM was more sensitive to carboplatin and cisplatin and the PARP inhibitors olaparib and niraparib than the *Brca1* wild-type PPNM and HR-proficient cell lines, BPCA, SPCA, and KPCA (Fig. 1E and F; Supplementary Fig. S2C and S2D). Of note, the *Trp53*-null cells (devoid of any other additional introduced mutations) were similarly sensitive to carboplatin and cisplatin treatments *in vitro* to the BPPNM cells.

Despite evidence in the literature suggesting that loss of *PTEN* sensitizes cells to PARP inhibitors (27–29), PPNM cells, which lack *PTEN* function, were not unusually sensitive to PARP inhibitors (Fig. 1F; Supplementary Fig. S2D). We also evaluated the CHK1 inhibitor prexasertib (LY2606368), which is known to trigger replication catastrophe (30) and

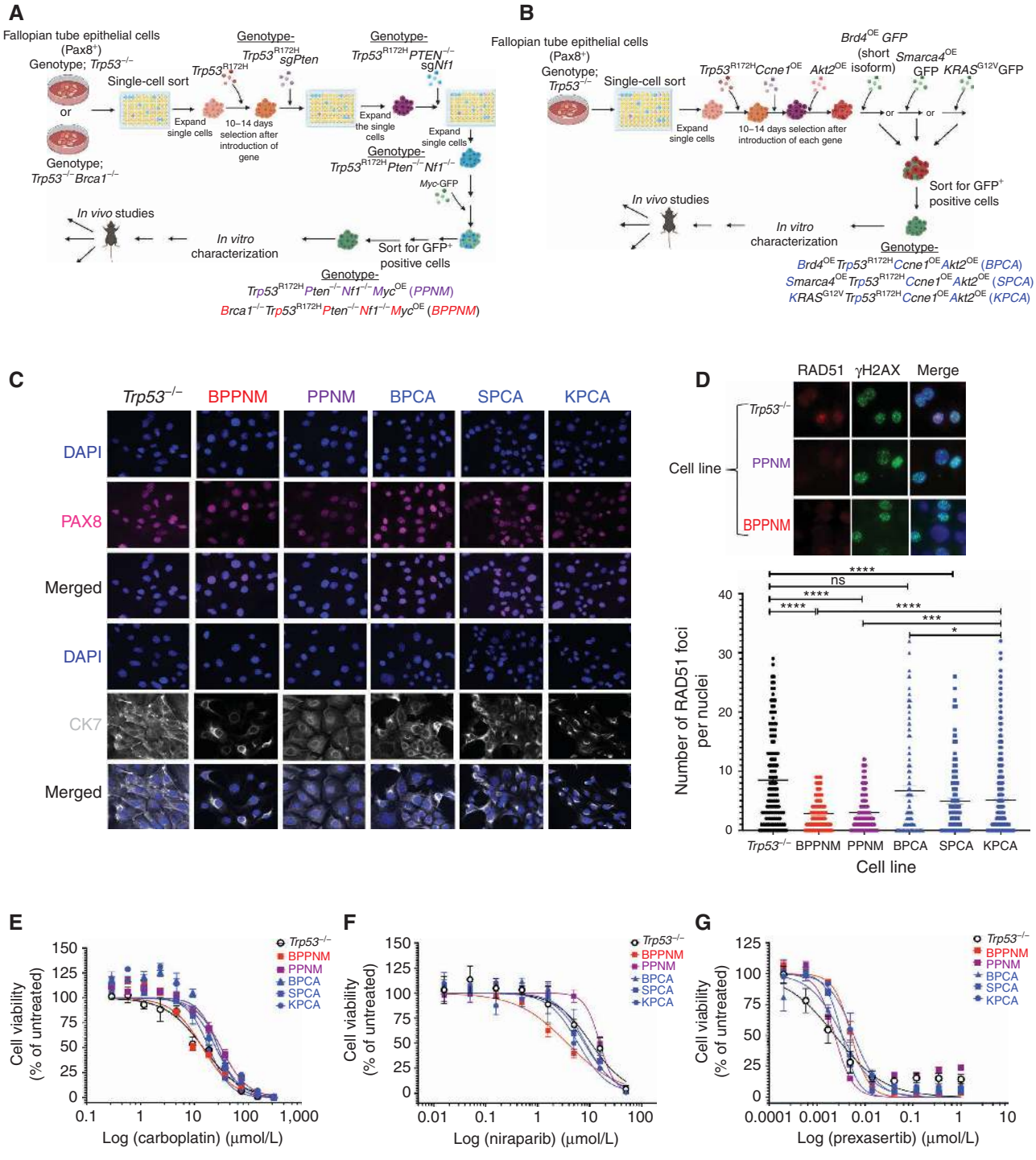

Figure 1. Engineering strategy and *in vitro* characterization of the murine FTE-derived cells. **A** and **B,** Schema showing the strategy for generation of (**A**) nonclassified and HR-deficient Pax8+ murine FTE-derived cells, *Trp53*$^{-/-R172H}$*Pten*$^{-/-}$*Nf1*$^{-/-}$*Myc*^{OE} (PPNM) and *Brca1*$^{-/-}$*Trp53*$^{-/-R172H}$*Pten*$^{-/-}$*Nf1*$^{-/-}$*Myc*^{OE} (BPPNM) and (**B**) HR-proficient Pax8+ murine FTE-derived cell lines *Trp53*$^{-/-R172H}$*Ccne1*^{OE}*Akt2*^{OE}*Brd4*^{OE} (BPCA), *Trp53*$^{-/-R172H}$*Ccne1*^{OE}*Akt2*^{OE}*Smarca4*^{OE} (SPCA) and *Trp53*$^{-/-R172H}$*Ccne1*^{OE}*Akt2*^{OE}*KRAS*^{G12V} (KPCA). **C,** Representative images showing immunofluorescence staining of nuclear PAX8 (pink) and cytoplasmic CK7 (white). Cell nuclei were stained with DAPI (blue). Images were taken with 63× magnification. **D,** Representative images showing immunofluorescence staining of RAD51 and γH2AX (top) and the quantification of the number of RAD51 foci per nuclei (bottom). Cell nuclei were stained with DAPI (blue). Images were taken with 63× magnification. **E-G,** Dose–response curves for *Trp53*$^{-/-}$, BBPNM, PPNM, BPCA, SPCA, and KPCA cells with the treatment of (**E**) carboplatin, (**F**) niraparib, and (**G**) prexasertib. Cell viability was calculated relative to 0.01% vehicle-treated control cells, measured with CellTiter-Glo assay 72 hours after treatment. Data depicted are pooled from two independent experiments. See also Supplementary Figs. S1 and S2.

is currently in clinical trials in patients with HGSC (31). We observed similar sensitivity to prexasertib in all of the lines with IC_{50} values of 2–6 nmol/L regardless of genotype (Fig. 1G). In the BRD4-overexpressing cell line (BPCA), we evaluated the responses to several BET bromodomain inhibitor/epigenetics targeting drugs, such as birabresib (OTX015), CPI-203, and JQ1. The BPCA cells were more sensitive to CPI-203 and JQ1 than the SPCA cells, with the A2780 human ovarian cancer cell line serving as a positive control (Supplementary Fig. S2E–S2G). The nonlinear regression analyses, including the IC_{50} for the drugs and cell lines mentioned above, are summarized in Supplementary Table S1. Given their faithful modeling of the drug sensitivities of the corresponding human diseases, we chose to focus on their *in vivo* characterization.

Engineered m-FTE Cells Recapitulate the Histopathologic and Clinical Features Seen in Patients with HGSC

We next sought to determine the engineered m-FTE cells' tumorigenic potential in immunocompetent C57BL/6 hosts (Fig. 2A). The HGSCs most often present clinically as metastases disseminated throughout the abdominal cavity (32, 33), recapitulated in our murine cell lines (Fig. 2B). The comparative Kaplan–Meier survival curves of mice bearing the genetically defined engineered cell lines are depicted in Fig. 2C and D and are summarized in Supplementary Table S2. We also confirmed that the BPPNM, PPNM, BPCA, SPCA, and KPCA tumors growing in syngeneic C57BL/6 hosts recapitulated typical HGSC histopathology (Supplementary Fig. S2H; Fig. 2E). We chose to focus on BPPNM, PPNM, and KPCA lines for further characterization in the work described below.

To begin, we determined the responses of host mice implanted with the BPPNM, PPNM, or KPCA cells and treated with either single-agent carboplatin (30 mg/kg), olaparib (50 mg/kg), or prexasertib (10 mg/kg; Fig. 2F). As expected, single-agent carboplatin was the most effective in the BPPNM tumor model, extending median survival to 116 days versus 56 days for the vehicle-treated controls ($P < 0.02$; Fig. 2G). Mice implanted with BPPNM cells also displayed a trend for a modest response to single-agent olaparib (median survival, 67 days) relative to the vehicle-treated control group (median survival of 56 days). In contrast, PPNM and KPCA did not exhibit any survival benefit in response to olaparib (Fig. 2H).

In the KPCA tumor–bearing mice, single-agent prexasertib elicited a statistically significant median survival prolongation to 46 days, relative to the vehicle-treated control group (median survival of 35 days, $P < 0.0038$). In contrast, mice bearing BPPNM and PPNM tumors did not exhibit any apparent beneficial response (Fig. 2I). These *in vivo* results (Fig. 2G and H) were consistent with the *in vitro* cytotoxicity responses of the BPPNM, PPNM, and KPCA cell lines (Supplementary Table S1) and supported the clinical fidelity of these models, including the chemotherapy resistance of the HR-proficient spectrum genotypes.

HGSC Tumors with Different Genotypes Evoke Distinct Immune Microenvironments

To characterize the cellular microenvironment of the BPPNM, PPNM, and KPCA models, we surveyed cell types and cell states using single-cell RNA sequencing (scRNA-seq; ref. 34; Fig. 3A; Supplementary Fig. S3A). In doing so, we identified transcriptionally distinct clusters corresponding to innate immune, adaptive immune, carcinoma, and stromal/nonimmune mesenchyme cell types (Fig. 3A and B) using previously described markers (see Supplementary Tables S3 and S4). In all three tumor models, omental metastases were dominated by cells identified as either neoplastic or myeloid with substantial proportions of stromal neutrophils and lymphoid cells (Fig. 3A and B). The scRNA-seq also indicated dramatically higher infiltration of myeloid cells in the BPPNM tumors, 44.5% compared with approximately 19.8%, and 24.3% in PPNM and KPCA tumors, respectively (inset of Fig. 3A).

We performed immune profiling and validation of the scRNA-seq at the protein level using multiparameter flow cytometry and IHC (Fig. 3C and D; Supplementary Fig. S3B–S3I, including flow cytometry gating strategies). The BPPNM tumors were the most inflamed, with elevated proportions of CD3e-positive T cells relative to PPNM tumors (2.3-fold higher, $P < 0.017$) and KPCA tumors (3.7-fold higher, $P < 0.0001$). The BPPNM tumors also exhibited elevated proportions of $CD8^+$ T cells relative to KPCA tumors (6.9-fold higher, $P < 0.004$). The BPPNM tumors were also heavily infiltrated with CD11c tumor–associated macrophages (TAM; ref. 35), which comprised 18% of all analyzed cells, a value that was significantly higher than PPNM (4.3-fold higher) and KPCA (2.6-fold higher) tumors. The KPCA tumors exhibited considerably higher proportions of $Ly6G^+Ly6C^+$ myeloid cells (3.5-fold higher, $P < 0.0175$) and $Ly6G^{lo}/Ly6C^{hi}$ monocytic myeloid cells (5.4-fold elevated relative in comparison with BPPNM tumors, $P < 0.0073$; Fig. 3C).

Exhaustion markers on $CD8^+$ T cells were coexpressed (36, 37) in all of the tumor types. However, highly exhausted $CD8^+$ T cells coexpressing PD-1, TIGIT, and TIM3 were significantly elevated in the KPCA tumors, comprising 31% of all $CD8^+$ T cells, a value nearly 10-fold higher than that observed in the BPPNM tumors ($P < 0.024$; Supplementary

Figure 2. *In vivo* characterization and drug sensitivity of the engineered murine FTE–derived BPPNM, PPNM, and KPCA cells. **A,** Genotypes of the engineered murine FTE–derived cell lines used for *in vivo* characterization. **B,** Representative images showing ascites and peritoneal metastasis formation in immune-proficient C57BL/6 mice after intraperitoneal injection with engineered murine FTE–derived cells. **C** and **D,** Kaplan–Meier curves showing percent probability of survival of mice injected with (**C**) $Trp53^{-/-R172H}$, $Trp53^{-/-R172H}Pten^{-/-}$, $Trp53^{-/-R172H}Nf1^{-/-}$, $Trp53^{-/-R172H}Pten^{-/-}Nf1^{-/-}$, PPNM, and BPPNM cells and (**D**) with $Trp53^{-/-R172H}$, $Trp53^{-/-R172H}Ccne1^{OE}Akt2^{OE}$, BPCA, SPCA, and KPCA cells. $n = 5$ or more/group. **E,** Representative images showing hematoxylin and eosin (H&E) staining and IHC analysis of indicated markers on harvested BPPNM, PPNM, BPCA, SPCA, and KPCA tumors. Scale bars, 200 μm. **F,** Experimental treatment strategy for single-agent carboplatin, olaparib, and prexasertib as two weekly doses via the intraperitoneal administration route for 4 weeks of duration. **G-I,** Kaplan–Meier curves showing percent probability of survival of mice injected with indicated engineered murine FTE–derived cell lines BPPNM, PPNM, and KPCA upon single-agent treatment with (**G**) carboplatin, (**H**) olaparib, and (**I**) prexasertib. $n = 5$ or more/group. A log-rank test compared the survival curves of individual groups to vehicle-matched control mice; ns, nonsignificant; *, $P < 0.05$; **, $P < 0.001$; ***, $P < 0.0001$. See also Supplementary Fig. S2.

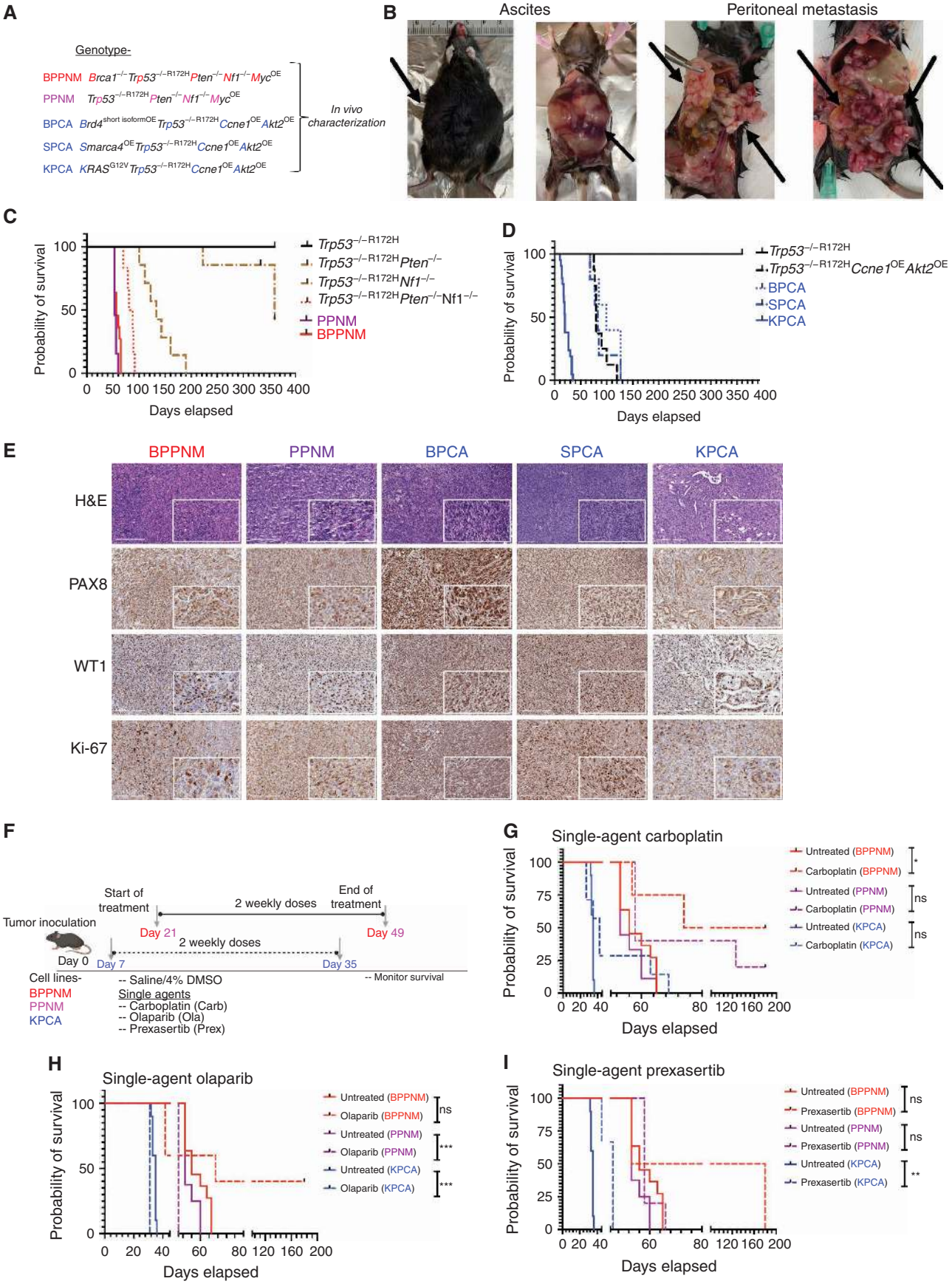

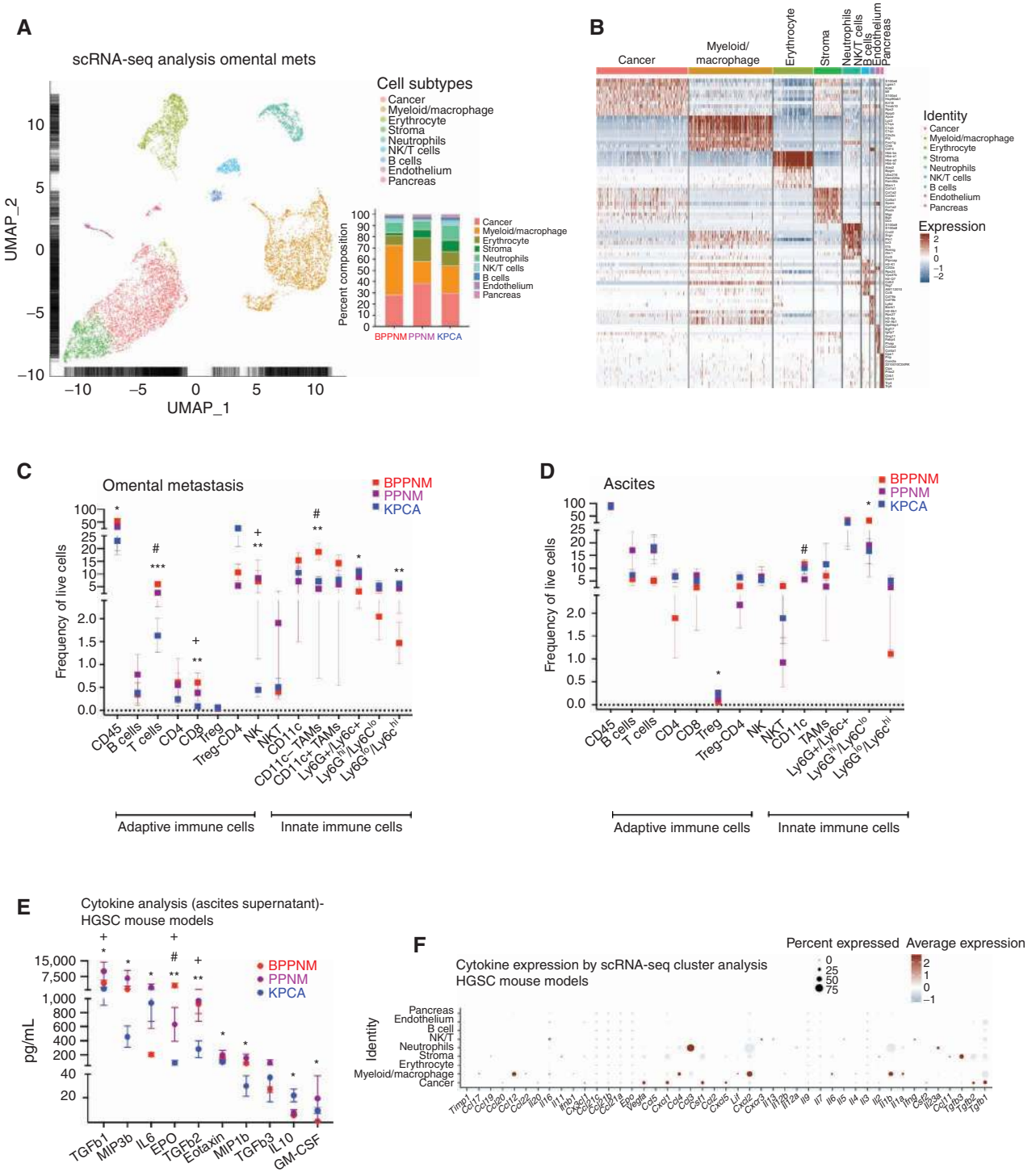

Figure 3. Cellular microenvironment analyses of omental tumors and ascites from BPPNM, PPNM, and KPCA tumor–bearing mice. **A,** UMAP plot of unbiased clustering the cellular components of merged BPPNM, PPNM, and KPCA omental tumors, where each color-coded cluster represents one cell type/state. Inset, relative composition of the clusters. Each point represents one cell that is colored by its cell type/state. **B,** Markers used to classify the clusters in **A** (see Supplementary Table S3 for details). **C** and **D,** Immunophenotypic analysis by multiparameter flow cytometry showing the frequency of live adaptive and innate immune cells of representative (**C**) omental tumors and (**D**) ascites derived from HGSC mouse models. **E,** Cytokine analysis of ascites supernatant HGSC mouse models. Data are presented as mean ± SEM; *, BPPNM vs. KPCA, + PPNM vs. KPCA, and # BPPNM vs. PPNM; *, $P < 0.05$; **, $P < 0.001$; ***, $P < 0.0001$, multiple *t* test. $n = 5$ or more/group. **F,** Depicts the transcript-level cytokines and chemokine expression within the omental tumors of the HGSC mouse models by scRNA-seq cluster analysis (**A** and **B**). See also Supplementary Figs. S3 and S4.

Fig. S3F). Altogether, these data indicated that T-cell suppression in BPPNM tumors is heavily influenced by myeloid cells, especially M2-like macrophages (Supplementary Fig. S3G). In contrast, $CD8^+$ T-cell function in KPCA tumors is suppressed via Tregs and immunosuppressive $Ly6G^+Ly6C^+$ myeloid cells (38). In addition to characterizing the immunophenotypes, we evaluated PD-L1 expression, which was elevated in the KPCA and BPPNM tumors relative to PPNM tumors, suggesting distinct genotype-driven immunosuppressive mechanisms. We also used IHC to confirm the results of our flow cytometry analysis (Supplementary Fig. S3H).

Each of the carcinoma cell genotypes also influenced the immune composition of the tumor-associated ascites (Fig. 3D). Thus, we observed distinct immune cell repertoires within ascites compared with the corresponding omental metastases, as observed in patients with HGSC (39). In particular, the ascites of the KPCA tumor–bearing mice were associated with the highest proportion of Tregs—almost 5-fold higher ($P < 0.037$) than in BPPNM ascites. The ascitic fluid in the BPPNM tumor–bearing mice was heavily infiltrated with $Ly6G^{hi}/Ly6C^{lo}$ granulocytes, which comprised nearly 33% of all cells, suggestive of a highly immunosuppressive immune microenvironment (38). By comparison, less than 17% of cells were $Ly6G^{hi}/Ly6C^{lo}$ granulocytes in the ascites of the KPCA tumor–bearing mice (Fig. 3D). The ascites from the PPNM tumor–bearing mice had elevated proportions of highly exhausted $CD8^+$ T cells coexpressing the PD-1, TIGIT, and TIM3 markers, in contrast to KPCA tumors (6.6-fold higher, $P < 0.00037$; Supplementary Fig. S3I), indicative once again of impaired effector T-cell functions (36, 37).

We also performed an extensive analysis of cytokines present in the conditioned media of the three cell lines propagated in culture. As we found, many cytokines were elevated in BPPNM culture supernatants relative to both PPNM and KPCA cell lines (Supplementary Fig. S4A and S4B). Consistent with BRCA1 deficiency in other models (40), there was a 6.5-fold elevation of IFNγ concentration in BPPNM relative to KPCA ($P < 0.001$) and a 9-fold elevation relative to PPNM ($P < 0.01$). Strikingly, higher levels of known drivers of myeloid and granulocytic chemotaxis and maturation cytokines were present in the BPPNM supernatant medium relative to those of the KPCA cell lines, including 280-fold higher GM-CSF ($P < 0.000006$), 30-fold more G-CSF ($P < 0.0001$), 20-fold more MCP1 ($P < 0.0002$), and an 80-fold elevation of MIP2 ($P < 0.0042$; Supplementary Fig. S4B). In light of these secreted cytokines' known biological effects, we concluded that the BPPNM cells, as gauged by their behavior *in vitro*, induce a strongly immunosuppressive tumor microenvironment *in vivo* composed of specific subsets of myeloid cells.

We compared the above data derived from analyses of conditioned media *in vitro* with the spectrum of cytokines in the ascitic fluid (39, 41) generated by the various tumor-bearing mice *in vivo*, which were quite distinct (Fig. 3E; Supplementary Fig. S4C). Thus, the ascites from the PPNM tumor–bearing mice contained the highest levels of TGFβ1, 7-fold elevated relative to ascites in KPCA tumor–bearing mice. In general, however, there were elevated levels of both TGFβ1 and TGFβ2 across the three cell lines (Fig. 3E). Ascites from BPPNM tumors contained increased concentrations of chemotactic factors relative to ascites formed by KPCA tumors, including MIP1β (2.7-fold, $P < 0.017$), eotaxin/CCL11 (1.5-fold, $P < 0.032$), and MIP3β (2.8-fold, $P < 0.011$). Ascites from KPCA tumors relative to BPPNM also contained elevated concentrations of immunosuppressive IL6 (4.6-fold higher, $P < 0.04$) and IL10 (4.4-fold higher, $P < 0.01$; Fig. 3E). The putative cellular source of the cell types responsible for secreting the cytokines highlighted above could be inferred from the scRNA-seq data, which suggested an outsized contribution of immunosuppressive, tumor-associated myeloid cells to the secretome, which are highly abundant in these tumors (Fig. 3F). Along with demonstrating dramatic effects of genotype on the spectrum of cytokines released by the various m-FTE cell lines, these analyses indicated that the behavior of these cells *in vitro* does not fully predict the secretory behavior of the corresponding tumors *in vivo*, which also include the contribution of stromal and immune cell types.

To determine whether the mouse models described here can recapitulate some of the cytokine profiles found in human HGSC tumors, we analyzed ascites of 10 patients with *BRCA1/2*-mutated HGSC and 7 patients with *CCNE1*-amplified HGSC (https://www.project-hercules.eu/). The ascites profiles showed seven cytokines differentially expressed (Supplementary Fig. S4D), and the profiles also showed high interpatient heterogeneity characteristic of HGSC. We next calculated fold changes of the cytokine expressions between the *BRCA1/2*-mutated and *CCNE1*-amplified human ascites samples and the corresponding fold changes between the BPPNM and KPCA mouse models. The heat map of this comparison is shown in Supplementary Fig. S4E. Both pairings show similar fold changes in 17 (65%) out of the 26 cytokines and opposite trends in nine. Of note, IL20 levels were significantly lower in *BRCA*-mutated compared with *CCNE1*-driven tumor ascites in both human and mouse samples.

Because cytokines are important mediators of the immune microenvironments, we examined the contribution of specific m-FTE–derived cytokines/chemokines that are thought to mediate the recruitment of specific immune cells to the tumor microenvironment. More specifically, we focused on evaluating the effect of functional blocking of GM-CSF and TGFβ 1/2/3 on BPPNM and TGFβ 1/2/3 on KPCA tumors using neutralizing antibodies. These cytokines were abundant in the conditioned media derived from cultures of the BPPNM and KPCA cell lines (Supplementary Fig. S4A and S4B). Using an *in vitro* Transwell chemotaxis assay, we evaluated their effects on immune cell migration (Supplementary Fig. S4F and S4G). In the case of the KPCA model, neutralization of TGFβ 1/2/3 reduced total $CD45^+$ lymphocyte migration relative to the control ($P < 0.03$; Supplementary Fig. S4H); however, no significant suppression of migration by myeloid cells was seen (Supplementary Fig. S4I). In the BPPNM model, neutralization of GM-CSF suppressed migration of total $CD45^+$ cells ($P < 0.008$) and $Ly6G^{hi}/Ly6C^{lo}$ granulocytes ($P < 0.01$; Supplementary Fig. S4J and S4K). Neutralization of TGFβ1/2/3 reduced the migration of $Ly6G^{hi}/Ly6C^{lo}$ granulocytes relative to the control ($P < 0.007$) and slightly increased macrophage migration relative to control ($P < 0.03$; Supplementary Fig. S4L and S4M). These findings were consistent with the known roles of GM-CSF and TGFβ as a chemoattractant for $CD45^+$ myeloid cells

and support the notion that genotype-driven differences in chemokine secretion by cancer cells can mediate recruitment of specific immune cell populations to the tumor microenvironment. Altogether, the scRNA-seq, flow cytometry, and ascitic cytokine data combined to describe distinct immunosuppressive microenvironments across the spectrum of the tumor cell genotypes compared here, this being reminiscent of the heterogeneity seen among tumors borne by patients with HGSC (42, 43).

Evaluating Optimal Combination Treatment Strategies in *BRCA1*-Null HGSC Tumors

We proceeded to evaluate the responses to certain commonly used targeted clinical therapies in the HR-deficient BPPNM and nonclassified PPNM tumor models. Prexasertib and olaparib combination proved synergistic *in vitro* for both the PPNM model (Bliss score = 1.8) and the BPPNM model (Bliss score = 1.01; Bliss scores greater than zero indicate synergy; Fig. 4A and B). *In vivo*, the combination of prexasertib and olaparib treatment demonstrated survival benefits in the BPPNM tumor–bearing mice (Fig. 4C and D, $P < 0.032$) and in the PPNM tumor–bearing mice (Fig. 4C and E, $P < 0.0054$).

Next, we proceeded to determine whether each model's genotype-driven drug sensitivities could be combined with ICB therapy. We observed elevated levels of PD-L1 expression in BPPNM tumors (Supplementary Fig. S3H), causing us to examine the impact of PD-L1 inhibition (44, 45) in combination with olaparib therapy (46, 47). In the BPPNM tumors, a significant extension of long-term survival was achieved using olaparib combined with anti–PD-L1 treatment. The vehicle-treated control group survived a median of 56 days, whereas 80% of the combination-treated mice survived more than 180 days. At that point, with no evidence of disease, the experiment was discontinued (Fig. 4C and D, $P < 0.0018$). Such significant survival benefit was not observed in the PPNM tumor–bearing mice, which carry wild-type *Brca1* alleles, suggesting that *Brca1* deficiency is necessary for responses to PARP inhibitors applied in combination with an ICB therapy. Based on these limited observations, we tentatively concluded that targeted therapy involving inhibition of the PARP pathway combined with an immune-checkpoint therapy in ovarian cancer offers the potential to tailor treatment for patients bearing *BRCA1*-defective HGSC tumors.

Growing evidence supports the important role of immune signatures associated with the HGSC tumor microenvironment as useful predictors of response to immunotherapies. To identify the tumor-associated immune signatures of *Brca1*-null BPPNM tumors (Fig. 4F) and the *Brca1*-wild-type–harboring PPNM tumors (Fig. 4G), we performed bulk-tumor RNA-seq. Differential expression analysis revealed extensive gene-expression differences between these tumors (Fig. 4H). Thus, we performed gene set enrichment analysis (GSEA) and cross-referenced these data with results emerging from the use of the Gene Ontology Consortium (GO) and Hallmark analyses (48). We also interrogated these differentially expressed genes to identify pathways that might have contributed to the differences observed in the responses to immunotherapies (Fig. 4H). Consistent with previous studies of HR-deficient HGSC patient cohorts (40, 49), IFNγ, IFNα, and inflammatory signatures were most upregulated in *Brca1*-null BPPNM tumors in comparison with *Brca1*–wild-type PPNM tumors. These IFN signatures likely contribute to the enhanced responses to ICBs, as observed in HR-deficient human HGSCs (40, 49). Hence, these models faithfully recapitulate these aspects of the human disease and may have broader implications for understanding the antitumor immune responses in *BRCA1*-null tumors.

Ccne1-Overexpressing HGSC Model Is Exquisitely Sensitive to Combinations of Cell-Cycle Checkpoint Kinase and Immune-Checkpoint Inhibitors

Studies combining genome-wide analysis and expression profiling in patients with HGSC have suggested that patients harboring *CCNE1* gene amplification driving overexpression of the encoded Cyclin E1 protein confront the worst overall survival (1, 50). This indicates the unmet clinical need to identify and target pathways associated with *CCNE1*-overexpressing HGSC tumors. We designed our therapeutic strategy to sensitize the KPCA tumor model, the cells of which overexpress *Ccne1* based on their modestly effective single-agent prexasertib response (as seen in Fig. 2I) and their immunosuppressive tumor microenvironment.

Initially, we chose to examine the impact of PD-L1 inhibition on reversing the observed T-cell dysfunction that could, we reasoned, have been caused by high levels of PD-L1 expression by the KPCA tumor cells (refs. 44, 45; Supplementary Fig. S3F and S3H). We additionally investigated CTLA4 inhibition (51), which can inhibit Treg function (elevated in KPCA tumors) and can promote T-cell infiltration (low in KPCA tumors; Fig. 3C and D). Single-agent anti–PD-L1 or anti-CTLA4 and combination anti–PD-L1 and anti-CTLA4 treatments were modestly effective, resulting in 46 days ($P < 0.003$), 51 days ($P < 0.033$), and 63 days ($P < 0.033$) median survival, respectively, in comparison with 35 days median survival of vehicle treatment control group (Fig. 5A–C).

We next evaluated the ability of carboplatin or prexasertib to sensitize the KPCA tumor model to these various checkpoint immunotherapies (ref. 52; Fig. 5A–K). The combination of carboplatin plus anti–PD-L1 and anti-CTLA4 therapies (termed here the CPC protocol) conferred a significant 140% increase in median survival time over the vehicle treatment control group (repeated in three independent cohorts, $P < 0.0005$). However, no complete long-term responses were achieved (Fig. 5B). Prexasertib administered together with anti–PD-L1 and anti-CTLA4 ICB in mice bearing KPCA tumors induced remarkable long-term tumor regression and overall survival benefit in the KPCA tumor model (Fig. 5C). Remarkably, the application of this triple-combination protocol (hereafter termed PPC) to the treatment of 12 mice bearing KPCA tumors resulted in a complete response in 10 mice (83% complete response rate, repeated in three independent cohorts, $P < 0.0001$). These responses were durable, being observed for 120 days after initiation of treatment. The depletion of $CD8^+$ cytotoxic

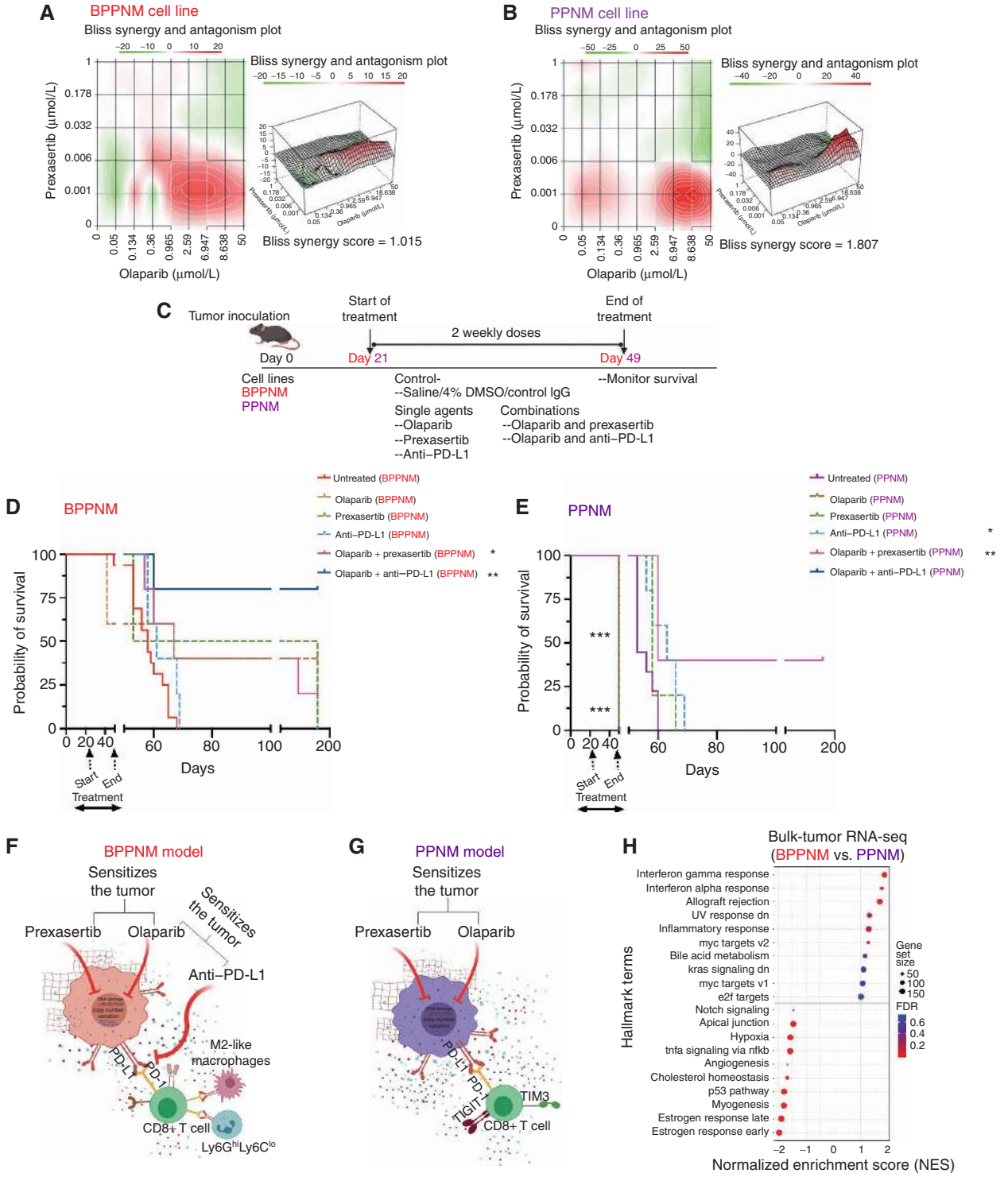

Figure 4. Evaluating optimal combination treatment strategies in BPPNM and PPNM tumor models. **A** and **B,** Synergy analysis of prexasertib and olaparib treatment in (**A**) BPPNM and (**B**) PPNM cell lines. Synergy and antagonism between the drugs were determined using SynergyFinder (see Methods for more details). Cell viability was calculated relative to 0.01% vehicle-treated control cells, measured with CellTiter-Glo assay 72 hours after treatment. Data depicted are pooled from two independent experiments. **C,** Experimental treatment strategy. **D** and **E,** Kaplan–Meier curves showing percent probability of survival of mice injected with engineered murine FTE–derived cell lines (**D**) BPPNM and (**E**) PPNM upon indicated treatment. $n = 5$ or more/group. A log-rank test compared the survival curves of individual groups to vehicle-matched control mice; *, $P < 0.05$; **, $P < 0.001$; ***, $P < 0.0001$. **F** and **G,** Cartoon models depicting (**F**) BPPNM and (**G**) PPNM tumor immune microenvironment and sensitization strategies. **H,** Bulk-tumor RNA-seq analysis showing enrichment of distinct hallmark terms in the *Brca1*-null HR-deficient ovarian model, BPPNM, and the nonclassified *Brca1* wild-type, PPNM model. The figure shows the categories enriched in each comparison. The x-axis shows the normalized enrichment score. Gene sets are shown on the y-axis. The dot size represents the number of genes from the ranked list present on each gene set, and the color indicates the FDR *q*-value.

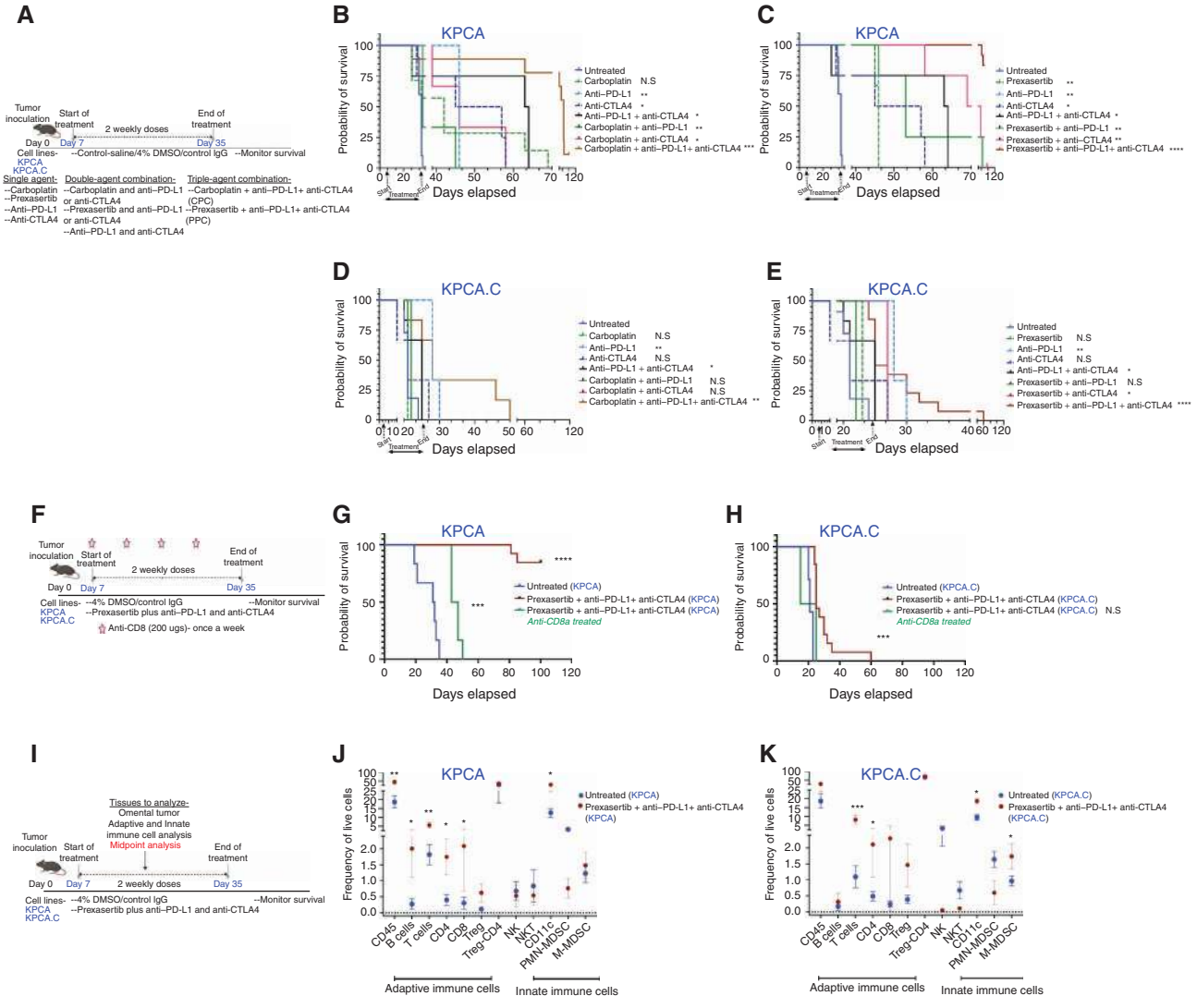

Figure 5. The sensitivity of HR-proficient *Ccne1*-overexpressing HGSC models to cell-cycle checkpoint kinase and immune-checkpoint inhibitors. **A,** Experimental treatment strategy. **B-E,** Kaplan–Meier curves showing percent probability of survival of mice injected with KPCA cell line (**B** and **C**) and KPCA.C cell line (**D** and **E**) upon indicated treatment. Data depicted are pooled from three independent experiments. A log-rank test compared the survival curves of individual groups to vehicle-matched control mice. $n = 5$ or more/group; *, $P < 0.05$; **, $P < 0.001$; ***, $P < 0.0001$. **F,** Experimental treatment strategy for the depletion of CD8$^+$ T cells using the anti-CD8 antibody. **G** and **H,** KPCA (**G**) KPCA.C (**H**) tumor–bearing mice with triple agents of prexasertib plus anti-PD-L1 and anti-CTLA4 combination therapies with or without anti-CD8 treatment. Data depicted are pooled from two independent experiments. A log-rank test compared the survival curves of individual groups to vehicle-matched control mice. $n = 5$ or more/group; *, $P < 0.05$; **, $P < 0.001$; ***, $P < 0.0001$. **I,** Experimental treatment strategy for midpoint immune analysis of omental tumor of KPCA and KPCA.C tumor–bearing mice treated with prexasertib plus anti-PD-L1 and anti-CTLA-4 combination therapies compared with vehicle-matched control mice. Immunophenotypic analysis by multiparameter flow cytometry shows the frequency of live adaptive and innate immune cells. **J** and **K,** KPCA (**J**) KPCA.C (**K**) omental tumors at midpoint mice treated with prexasertib plus anti-PD-L1 and anti-CTLA4 combination therapies compared with vehicle-matched control mice. Data are presented as mean ± SEM, *t* test; *, $P < 0.05$; **, $P < 0.001$; ***, $P < 0.0001$. Data depicted are pooled from two independent experiments. See also Supplementary Figs. S5 and S6.

T cells before treatment with this PPC therapy prevented complete responses, with only a small increase in median survival retained, highlighting the critical contribution of CD8$^+$ T cells (Fig. 5F and G).

We next interrogated the memory T-cell response in surviving tumor-free mice by rechallenging six mice with the same KPCA cell line (at least seven months after last therapy, $N = 6$). All mice that had previously exhibited a complete response rejected the rechallenge (survival >2.5 months), whereas all tumor-naïve mice succumbed to disease ($P < 0.0022$; Supplementary Fig. S5A). Together, these data indicated that CHK1 inhibition by prexasertib in the KPCA tumors induced a strong response to dual ICB therapy that depended on CD8$^+$ T cells and was capable of producing long-term immunologic memory to the KPCA tumors.

Spontaneous Resistance to Triple-Combination Therapy in Clones of the *Ccne1*-Overexpressing HGSC Model May Be Driven by Follistatin Overexpression in Cancer Cells

Given the robust responses of KPCA tumors to the triple PPC therapy, we decided to evaluate its efficacy in a second independently derived FTE clone bearing the same introduced genetic lesions as the KPCA cell line studied above; we term this second line KPCA.C hereafter (Fig. 1B). We confirmed the presence of genetic alterations in the KPCA.C cell line that replicated those present in the KPCA cells (Supplementary Fig. S5B–S5D). We also compared the genetic similarity of KPCA.C cells to KPCA cells using whole-exome sequencing (WES) analysis (Supplementary Fig. S5E) and assessed allelic imbalance profiles using shallow WGS (Supplementary Fig. S5F and S5G). No apparent differences were observed in examining the genetic similarity of KPCA.C cells to KPCA cells. We also showed that KPCA.C cells exhibited a similar response to prexasertib *in vitro* in terms of DNA damage induction and replication stress (30), as seen in the related KPCA cell line (Supplementary Fig. S5H). Additionally, we confirmed the HGSC cancer histopathology features of KPCA.C-induced tumors (Supplementary Fig. S5I).

However, although we observed significant responses of the KPCA tumors, both the CPC treatment (Fig. 5D) and PPC therapy (Fig. 5E) of the closely related KPCA.C tumors yielded only very modest therapeutic responses. The CPC (28 days, $P < 0.001$) and PPC (26 days, $P < 0.0001$) extended median survival over vehicle control (21 days) only incrementally (results of three independent experiments).

The depletion of $CD8^+$ T cells before PPC therapy of the KPCA.C cells eliminated even the modest increase in survival produced by PPC (Fig. 5F–H), suggesting that even this modest response depended on $CD8^+$ T cells. Collectively, all mice treated with PPC showed a modest antitumor response and were sacrificed due to excessive tumor burden. Thus, the KPCA.C tumors, in contrast to the closely related KPCA, were largely resistant to combination prexasertib plus anti–PD-L1 and anti-CTLA4 blockade therapies (Fig. 5C and E).

We then sought to identify the factors driving the KPCA and KPCA.C populations' differential responses to PPC therapy. Multiparameter flow cytometry monitoring immune cells revealed modest differences in tumors seeded by each clone (Supplementary Fig. S6A–S6D). Thus, the KPCA.C tumors were associated with a higher proportion of immunosuppressive Tregs in both the omental tumors (3.2-fold more, $P < 0.04$) as well as in the ascites (3-fold more, $P < 0.02$) relative to the KPCA tumors (Supplementary Fig. S6A–S6C). The KPCA tumors were infiltrated with more $Ly6G^{hi}/Ly6C^{lo}$ granulocytes (2.4-fold higher, $P < 0.03$) in comparison with KPCA.C tumors (Supplementary Fig. S6A). The ascites of the KPCA tumor–bearing mice contained far more $CD8^+$ T cells (3.8-fold more, $P < 0.02$) relative to the ascites generated by the KPCA.C tumors. In contrast, the KPCA omental tumors had higher levels of exhausted TIGIT- and TIM3-positive $CD8^+$ T cells relative to KPCA.C tumors (1.5-fold more, $P < 0.035$; Supplementary Fig. S6C and S6D). These observations suggest complex differences between the immune microenvironments of KPCA versus KPCA.C tumors.

The differences in immune populations in the tumors generated by each clonal population were also assessed following treatment with PPC (Fig. 5I–K). Thus, omental tumors were harvested and weighed midway through the typical treatment regimen with PPC before undergoing flow cytometry analysis (Fig. 5I–K; Supplementary Fig. S6E and S6F). In consonance with the survival data, tumor weight decreased after treatment with PPC for the KPCA clone, but not for KPCA.C when relative to untreated control (Supplementary Fig. S6F). PPC treatment drove an influx of immune cells into both the KPCA and the KPCA.C tumors; however, the KPCA tumors were infiltrated by more immunocytes with smaller proportions of immunosuppressive cells (Fig. 5I–K).

Given the lack of apparent differences in the genomes between the KPCA and KPCA.C cell lines based on the whole-exome and shallow WGS analysis (Supplementary Fig. S5F–S5H), we hypothesized that differences in gene expression might drive the differential response seen in the KPCA (exceptional responders) and KPCA.C tumors (partial responders). To test this notion, we performed bulk RNA-seq on both types of tumors. Bulk RNA-seq of tumors derived from each clone revealed extensive gene-expression differences. We interrogated these differentially expressed genes to identify pathways that might have contributed to the treatment resistance of the KPCA.C tumors (Fig. 6A). Furthermore, we performed scRNA-seq to compare cell types and cell states between KPCA and KPCA.C, doing so to identify potential differences underlying the more immunosuppressive omental tumor microenvironment of the KPCA.C tumors (Fig. 6B; Supplementary Fig. S7A; Supplementary Tables S3 and S5).

We initially focused our attention on gene-expression differences between KPCA and KPCA.C associated with the cancer cell cluster identified in the scRNA-seq data set (Fig. 6C). More specifically, we identified as high-priority candidate genes significantly overexpressed in the therapy-resistant KPCA.C tumors relative to the exceptional responders in the KPCA-bearing cohort. We also validated the overexpression of these genes in the cancer cell lines *in vitro*. To further restrict our candidate list to potentially actionable immunotherapeutic targets, we performed GSEA and cross-referenced these data to results emerging from the use of the GO and Hallmark analyses (48) to identify immune-modulating secreted factors.

Using the above analytic methods, we prioritized the following three candidate gene targets: *Fst, S100a4*, and *Il33* (Fig. 6D; Supplementary Fig. S7B and S7C). When comparing cell culture supernatants of the KPCA.C cell lines relative to those of their KPCA counterparts, we confirmed the elevated expression of follistatin (FST; Fig. 6E) by ELISA. The KPCA.C cells exhibited a 7.5-fold elevated expression of FST compared with KPCA cells (Fig. 6E). We then tested the hypothesis that KPCA but not KPCA.C could further upregulate FST expression in response to TGFβ, a potent inducer of this pathway (53, 54). Strikingly, following TGFβ stimulation, KPCA.C cells exhibited

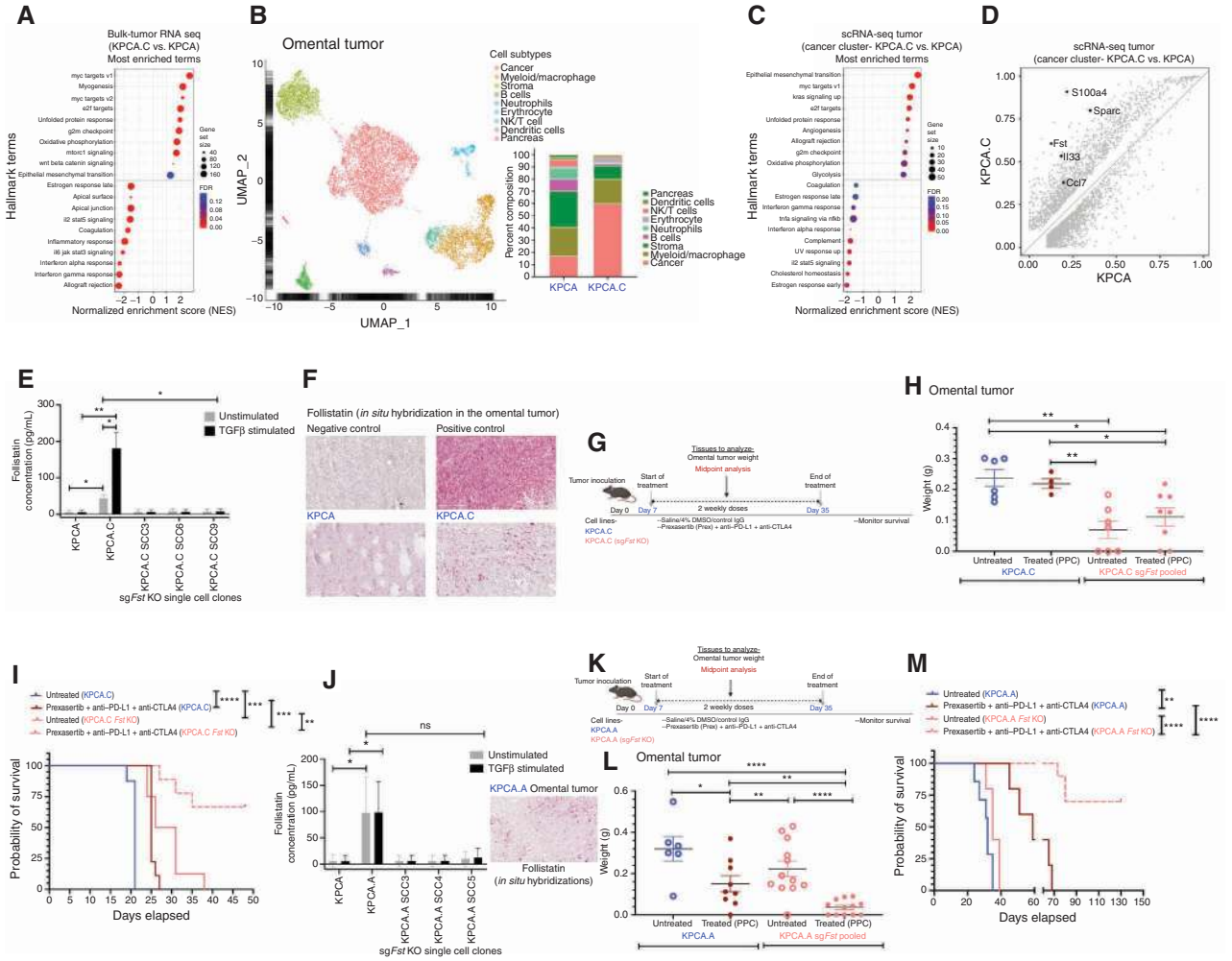

Figure 6. Identification and ablation of Follistatin in the *Ccne1*-overexpressing KPCA.C model to sensitize the tumor to cell-cycle checkpoint kinase and immune-checkpoint inhibitors. **A,** Bulk-tumor RNA-seq analysis showing enrichment of distinct hallmark terms in *Ccne1*-overexpressing ovarian models. The figure shows the categories enriched in each comparison. The x-axis shows the normalized enrichment score. Gene sets are shown on the y-axis. The dot size represents the number of genes from the ranked list present on each gene set, and the color shows the FDR *q*-value. **B,** UMAP plot of unbiased clustering the cellular components of merged KPCA and KPCA.C omental tumors, where each color-coded cluster represents one cell type/state. Inset, relative composition of the clusters. Each point represents one cell that is colored by its cell type/state. **C,** scRNA-seq analysis showing enrichment of distinct hallmark terms in *Ccne1*-overexpressing ovarian models. The figure shows the categories enriched in each comparison. The x-axis shows the normalized enrichment score. Gene sets are shown on the y-axis. The dot size represents the number of genes from the ranked list present on each gene set, and the color shows the FDR *q*-value. **D,** Cancer cluster identified by scRNA-seq of KPCA.C and KPCA omental tumors, depicting genes upregulated in KPCA.C tumors versus KPCA tumors. **E,** FST concentration in cell culture supernatants taken from KPCA and KPCA.C cell lines and KPCA.*sgFstKO* single-cell clones. **F,** *In situ* hybridization of FST on omental tumor sections derived from KPCA and KPCA.C ovarian models using RNAscope methodology (pink = FST). Scale bars, 200 μm. **G,** Experimental treatment strategy for midpoint analysis. **H,** Comparing omental tumor weights of untreated and prexasertib plus anti–PD-L1 and anti-CTLA4 combination therapy-treated KPCA.C or KPCA.C *sgFstKO* cohorts. **I,** Kaplan–Meier curves showing percent probability of survival of mice injected with KPCA.C or KPCA.C *sgFstKO* cell line upon indicated treatment. A log-rank test compared the survival curves of individual groups to vehicle-matched control mice. $n = 5$ or more/group; *, $P < 0.05$; **, $P < 0.001$; ***, $P < 0.0001$. The data depicted are pooled from two independent experiments. **J,** FST concentration in cell culture supernatants taken from KPCA and KPCA.A cell lines, and KPCA.A *sgFstKO* single-cell clones. *In situ* hybridization of FST on omental tumor section derived from KPCA.A ovarian model using RNAscope methodology (pink = FST). Scale bar, 200 μm. **K,** Experimental treatment strategy for midpoint analysis. **L,** Comparison of omental tumor weights of untreated and prexasertib plus anti–PD-L1 and anti-CTLA4 combination therapy-treated KPCA.A or KPCA.A *sgFstKO* cohorts. **M,** Kaplan–Meier curves showing the percent probability of survival of mice injected with KPCA.A or KPCA.A *sgFstKO* cell line upon indicated treatment. A log-rank test compared the survival curves of individual groups to vehicle-matched control mice. $n = 5$ or more/group; *, $P < 0.05$; **, $P < 0.001$; ***, $P < 0.0001$. The data depicted are pooled from two independent experiments. See also Supplementary Fig. S7.

a 32-fold greater elevation of expression of FST compared with KPCA by ELISA (Fig. 6E). To examine the possible functions of S100A4 and IL33 in the observed differences in therapeutic responses, we generated knockouts of the *S100a4* and *Il33* genes in the genome of cells of the KPCA.C line using the CRISPR/Cas9 approach. Here, we observed only modest differences in survival with PPC blockade therapies when comparing the survival of the *S100a4*- or *Il33*-knockout (KO) tumors relative to their matched controls (Supplementary Fig. S7D and S7E).

We then focused our analyses on the third gene of possible interest, which encodes *Fst*, an autocrine glycoprotein that primarily binds and bioneutralizes members of the TGFβ superfamily (55). FST has been used clinically as a marker for the shorter overall survival of patients with ovarian cancer (56). FST is an inhibitor of activin involved in the regulation of myeloid (57), dendritic, and T-cell functions (58). We confirmed the elevated expression of FST in KPCA.C tumors in comparison with KPCA in the omental tumors using RNA *in situ* (RNAscope) methodology (ref. 59; Fig. 6F).

To uncover the possible functional contributions of *Fst* to the observed therapeutic responses, we generated a knockout of the *Fst* gene in the genome of the KPCA.C cells using the CRISPR/Cas9 approach. We confirmed the loss of its encoded product by ELISA of medium supernatants generated by the KO cells (Fig. 6E). We then treated mice bearing KPCA.C *Fst* KO tumors with the triple PPC blockade therapy protocol (see treatment regime in Fig. 6G) and compared the overall survival to untreated matched controls. We also measured omental tumor weights at the treatment's midpoint time point and compared them with the untreated cohorts (Fig. 6H, repeated in two independent cohorts). In the *Fst* KO cells (*sgFst* pool) untreated cohort, we observed a median survival of 28.5 days ($P < 0.0001$; Fig. 6I) in comparison with a median survival of 21 days in parental untreated KPCA.C tumor–bearing mice. Remarkably, tumor regression and highly significant overall survival benefit were observed in the triple combination of PPC blockade therapies in the *Fst* KO tumors (*sgFst* pool). Of the nine KPCA.C *Fst* KO tumor–bearing mice treated with the triple combination, six mice exhibited a complete response observed for 48 days following treatment ($P < 0.0001$, Fig. 6I, repeated in two independent cohorts). This contrasts with the behavior of KPCA.C tumor–bearing mice, which were largely resistant to triple PPC blockade therapy.

Given the robust responses of *Fst* KO KPCA.C tumors to the triple PPC therapy, we decided to evaluate its efficacy in yet another independently derived FTE clone bearing the same introduced genetic lesions as the KPCA and KPCA.C cell line; we term this cell line KPCA.A hereafter. We confirmed the presence of genetic alterations (Supplementary Fig. S5B–S5D), and compared the genetic similarity of KPCA.A cells with KPCA cells using WES analysis (Supplementary Fig. S5E) and WGS (Supplementary Fig. S5F and S5G). In the WES analysis, we observed some differences at the single-nucleotide level between KPCA.A and KPCA cells (denoted in blue, Supplementary Fig. S5E; Supplementary Table S6). Besides, we showed that KPCA.A cells exhibited a response to prexasertib *in vitro* in terms of DNA damage induction and replication stress (30), similar to that seen in the related KPCA cell line (Supplementary Fig. S5H). Additionally, we confirmed the HGSC histopathology features of KPCA.A-induced tumors (Supplementary Fig. S5I).

Similar to our approach described earlier, we confirmed the elevated expression of FST by ELISA (Fig. 6J) and *in situ* (RNAscope) methodology (Fig. 6J, inset). Similar to our approach with the KPCA.C cells, we generated a knockout of the *Fst* gene in the genome of the KPCA.A cells using the CRISPR/Cas9 approach and confirmed the loss of its encoded product by ELISA (Fig. 6J). We then treated mice bearing KPCA.A *Fst* KO tumors with the triple PPC blockade therapy protocol (see treatment regime in Fig. 6K) and compared the overall survival with untreated matched controls. We measured omental tumor weights at the treatment's midpoint time point and compared them with the untreated cohorts (Fig. 6L, repeated in two independent cohorts). Remarkably, tumor regression and highly significant overall survival benefit were observed in the triple PPC therapy in the *Fst* KO tumors (sg*Fst* pool). Of the ten *Fst* knockout KPCA.A tumor–bearing mice treated with the triple combination, seven mice exhibited a complete response and remarkable long-term survival for more than 130 days following treatment ($P < 0.0001$; Fig. 6M, repeated in two independent cohorts). We concluded that FST functioned as a potent driver of the observed resistance to the triple PPC treatment protocol of KPCA.C and KPCA.A tumors.

To further unravel the molecular basis of *Fst* overexpression in the PPC therapy–resistant KPCA.C and KPCA.A clones, we assessed copy-number changes at the *Fst* loci using shallow whole-genome analysis (Supplementary Fig. S7F). We did not observe an amplification in the KPCA.C and KPCA.A model or deletion KPCA models in the *Fst* locus. Given the lack of apparent genetic differences at the *Fst* locus among the three cell lines, i.e., KPCA, KPCA.A, and KPCA.C, we hypothesized that the differential response seen in the KPCA (exceptional responders) and KPCA.C and KPCA.A (partial responders) tumors might be driven by an epigenetic mechanism. To explore this possibility, we analyzed chromatin accessibility by Assay for Transposase-Accessible Chromatin using sequencing (ATAC-seq) in KPCA, KPCA.C, and KPCA.A models at the *Fst* locus (Fig. 7A). We observed evidence of epigenetic regulation of *Fst* regulatory elements concordant with the expression data (Fig. 7B).

The observations suggested that FST expression can serve as a predictive biomarker for both ICB and prexasertib combination treatment response; accordingly, we assessed the effects of *Fst* overexpression (OE) in the PPC treatment–responsive KPCA model. For this purpose, we overexpressed *Fst* in KPCA cell lines by lentiviral vector transduction and confirmed the elevated FST levels of the cell culture supernatants by ELISA (Fig. 7C). We then treated KPCA *Fst* OE tumor–bearing mice with the combination treatment PPC (Fig. 7D). Indeed, forced *Fst* overexpression reversed the PPC treatment sensitivity of the KPCA tumors (Fig. 7D). Median survival was significantly reduced to 50 days in PPC-treated KPCA *Fst* OE tumor–bearing mice, compared with more than 120 days long-term overall survival in KPCA models undergoing the same combination treatment, $P < 0.0001$ (Fig. 7D, repeated in three independent cohorts). We concluded that elevated levels of FST are sufficient, on their own, to induce resistance to the combination treatment of PPC in previously sensitive KPCA models.

Furthermore, differential expression analysis between KPCA *Fst* OE and KPCA tumors revealed extensive gene-expression differences between these tumors (Fig. 7E) that might have broader utility in mounting an antitumor immune response.

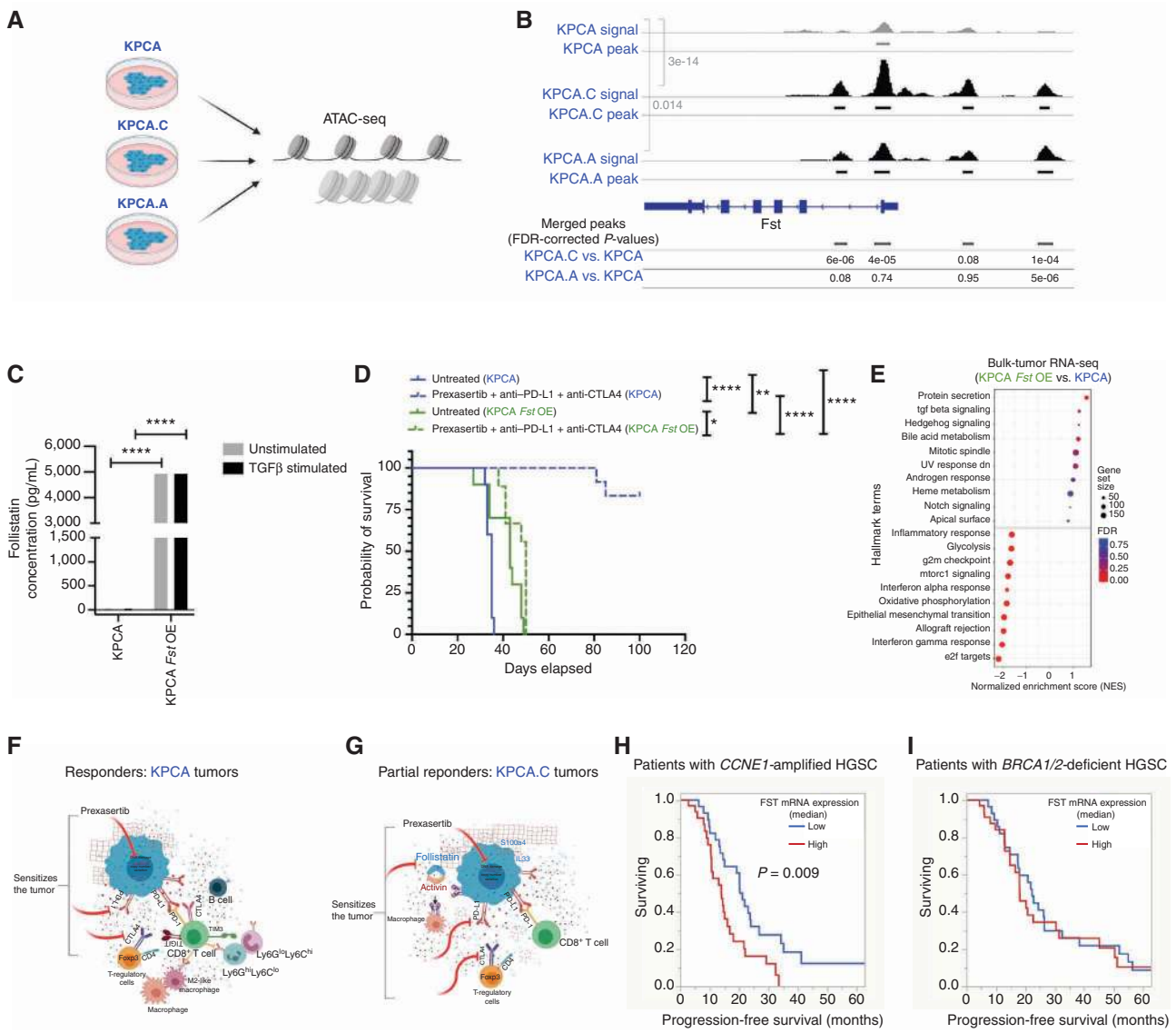

Figure 7. Epigenetic features and FST overexpression in *Ccne1*-overexpressing model. **A,** Schema depicting ATAC-seq experimental setup using KPCA, KPCA.C, and KPCA.A cell lines. **B,** Chromatin accessibility (ATAC-seq read pileups) in the *Fst* genomic region. Comparisons are shown for each peak and all four peaks together. **C,** FST concentration in cell culture supernatants taken from KPCA and KPCA *Fst* overexpression (OE) cell lines. **D,** Kaplan–Meier curves showing percent probability of survival of mice injected with KPCA or KPCA *Fst* OE cell line upon indicated treatment. A log-rank test compared the survival curves of individual groups to vehicle-matched control mice. $n = 5$ or more/group; *, $P < 0.05$; **, $P < 0.001$; ***, $P < 0.0001$. The data depicted are pooled from three independent experiments. **E,** Bulk-tumor RNA-seq analysis showing enrichment of distinct hallmark terms in KPCA *Fst* OE and KPCA tumors. The figure shows the categories enriched in each comparison. The x-axis shows the normalized enrichment score. Gene sets are shown on the y-axis. The dot size represents the number of genes from the ranked list present on each gene set, and the color shows the FDR q-value. **F** and **G,** Cartoon models of (**F**) KPCA-exceptional responder and (**G**) KPCA.C-partial responder tumors depicting tumor immune–microenvironment and sensitization strategies. **H,** Kaplan–Meier curves depicting PFS in patients with *CCNE1*-amplified HGSCs grouped to high and low by median FST mRNA expression). **I,** Kaplan–Meier curves depicting PFS in patients with *BRCA1/2*-deficient HGSCs grouped to high and low by median *FST* mRNA expression (see Methods for details). See also Supplementary Fig. S7.

Collectively, the *Ccne1*-overexpressing KPCA and KPCA.C models (Fig. 7F and G) and KPCA.A uncovered that inhibition of CHK1 potentiates immune-checkpoint response in an FST-dependent manner.

Given that high FST expression could be found to drive treatment resistance in the *Ccne1*-overexpressing mouse model, we next examined whether FST expression could predict progression-free survival (PFS) for platinum-based chemotherapy in human HGSCs using the TCGA data set (1). Intriguingly, high FST expression significantly predicted shorter PFS selectively in patients with *CCNE1*-amplified HGSCs (Fig. 7H; $P = 0.0009$, log-rank test), but not among the patients with *BRCA1/2*-deficient tumors (Fig. 7I). High FST expression significantly predicted shorter PFS in the

CCNE1-amplified tumor cohort as a continuous variable [hazard ratio (HR) 19.7, 95% CI, 3.8–109.9, $P = 0.0003$], and also independently after adjusting for tumor stage and patient age at diagnosis (HR 24.4, 95% CI, 4.8–133.6, $P = 0.0001$). The overall survival showed a similar trend (Supplementary Fig. S7G and S7H).

These data provide a strong indication that FST overexpression, which is common in HGSCs and is clinically associated with shorter overall survival, may limit clinical responses of HGSC tumors to checkpoint blockade immunotherapy. Therefore, FST may represent an important target of inhibition undertaken to potentiate the clinical utility of ICB therapies of patients with HGSC.

DISCUSSION

The currently available therapies applied to the treatment of ovarian carcinomas are limited in their efficacy, in part because these tumors constitute a heterogeneous disease with a number of distinct mutant genotypes that exert varied, poorly understood effects on the tumor phenotype, including its microenvironment and drug response. This heterogeneity has been particularly challenging when evaluating new immunotherapies, given our lack of understanding of how cancer genotypes drive both immunophenotypes and therapeutic responses.

In this study, we generated a series of genetically defined mouse HGSC cells lines that (i) were derived from FTE cells—the presumed normal cells of origin of HGSCs (17–19); (ii) carry constellations of mutant alleles present in human HGSC genomes; and (iii) form tumors in syngeneic immunocompetent C57BL/6 mice. Our central goal in this effort was to determine how alternative genotypes of HGSCs growing in syngeneic hosts govern the composition of tumor-associated immune microenvironments and modulate the responsiveness to currently available immunotherapies. With these models in hand, we hope to enable future studies by ourselves and others focused on determining the influence of various genomic states on the tumor microenvironment, clinical progression, and treatment responses.

The strength of our models is that the mutations used capture some of the most prominent pathways dysregulated in HR-deficient and HR-proficient HGSC patient samples. These genetically defined engineered m-FTE cell lines recapitulated the histology and clinical behavior of human HGSCs in their spread through the peritoneal cavity, their preferential adhesion to intraperitoneal sites including the omentum, and their responsiveness to both DNA-damaging agents and PARP inhibitors. The clinical fidelity of these murine models was further supported by the increased responses to platinum-based reagents (carboplatin and cisplatin), as well as PARP inhibitors (olaparib and niraparib), in the *Brca1* mutant, HR-deficient cell line. By contrast, the DNA-damaging therapies afforded little improvement in the overall survival of HR-proficient HGSC genotypes, reflecting the poor treatment responses also observed in the clinical setting. Notably, preclinical models recapitulating the complex biology of *CCNE1*-driven HGSC tumors have not been available until now, highlighting the potential of the presently described models to answer a clinically unmet need for improved therapeutic options for patients with HR-proficient HGSCs.

We initiated studies to explore the dynamic interplay between various genetically defined tumor models and the corresponding tumor-associated immune microenvironments that they recruit. In our hands, the comprehensive analyses of the omental tumor microenvironments revealed distinct immune landscapes associated with different tumor genotypes. Somewhat unsurprisingly, the tumors with deficient HR DNA repair (BPPNM) were most heavily infiltrated with immune cells, suggesting a more immunogenic phenotype. These tumors carried the highest proportions of CD3e-positive T cells, highly exhausted $CD8^+$ T cells, M2-like macrophages, and the lowest proportion of Tregs. These differences correlated with elevated levels of cytokines known to drive T-cell suppression and myeloid cell infiltration, including MIP3β, TGFβ1, and TGFβ2 (60–62). Notably, the immunologic signatures detected in human tumors (40, 49) resembled the cytokine and gene-expression profiles of the genetically defined HR-deficient mouse models described in this study.

Heavily inflamed tumors of other tumor types expressing high PD-L1 levels are often considered as useful predictive indicators of successful ICB therapies in the clinic (63). However, BPPNM tumors were unresponsive to single-agent PD-L1 and produced long-term survival only when ICB was combined with olaparib, reflecting reported clinical data (46, 49, 63). These data suggest that PD-L1 expression and inflammatory status may not be sufficient on their own to predict the success of ICB in these tumors and that immune-stimulating alterations to the tumor microenvironment incurred by adjuvant treatments such as chemotherapy may be necessary for a significant response to checkpoint inhibitors (43, 64). Nonetheless, more generally, targeted therapy based on inhibiting the DNA damage response pathway in combination with ICB therapy in ovarian cancer offers the potential to tailor treatment for patients with *BRCA1*-mutant HGSC.

The HR-proficient KPCA tumors displayed a more immunosuppressive microenvironment than that assembled by the BPPNM tumors and exhibited an entirely different response to immunotherapeutic combinations. The KPCA tumors, which showed high PD-L1 expression, were poorly infiltrated with T cells and had higher proportions of exhausted $CD8^+$ cells coexpressing PD-1, TIGIT, and TIM3, comprising 31% of all $CD8^+$ cells—a value nearly 10-fold higher than that of BPPNM tumors. The KPCA tumors were also infiltrated with higher proportions of immunosuppressive cells, including Tregs, $Ly6G^+Ly6C^+$ myeloid cells, and $Ly6G^{lo}/Ly6C^{hi}$ monocytic myeloid cells (38). The ascites of KPCA tumor–bearing mice also contained elevated levels of many cytokines known to be immunosuppressive, such as TGFβ and IL10 (41, 62, 65–67). Single and double combinations of anti-CTLA4, anti–PD-L1, carboplatin, olaparib, and prexasertib were all mostly ineffective in treating these tumors. However, a triple combination of anti-CTLA4, anti–PD-L1, and prexasertib showed remarkable benefits, including complete responses that were dependent on the presence of cytotoxic $CD8^+$ T cells. Collectively, these data may presage a use for CHK1

inhibition by prexasertib to potentiate ICB efficacy in *CCNE1*-amplified HGSCs.

The behavior of the KPCA.C and KCPA.A variant clones, which were relatively resistant to the same triple-combination therapy involving prexasertib plus anti–PD-L1 and anti-CTLA4 that eliminated the related KPCA tumors, was unanticipated, if only because they ostensibly carry the same genetic alterations as KPCA cells. A comparison of gene expression between these differentially responding variant clones identified *Fst* as a potential determinant of resistance that was further pursued, leading eventually to the identification of *Fst* as an important determinant of responsiveness to the triple therapy described here. Furthermore, to understand the molecular basis of *Fst* overexpression in the PPC treatment–resistant KPCA.C and KCPA.A cells, we investigated epigenetic differences between these cells and compared them with the PPC treatment–sensitive KPCA cell line. We identified putative *Fst* regulatory elements using ATAC-seq that might underlie its overexpression. Rigorous overexpression studies confirmed *Fst* is an important determinant of therapeutic response.

The precise mechanisms of action of *Fst* and its contribution to the immunosuppressive microenvironment of KPCA.C tumors are unclear at present. FST is a secreted inhibitor of activin, a TGFβ family ligand previously linked to shorter overall survival in ovarian cancer (56, 68). FST can also bind and regulate other TGFβ family ligands such as myostatin, and BMPs, albeit with lower affinity (54, 69). Knocking out FST expression in the previously resistant KPCA.C and KPCA.A tumor cells restored much of the efficacy of the triple combination, with a majority of tumor-bearing hosts showing a complete response. Given the reported function of activin in regulating myeloid cells, which are abundant in these tumors (57, 58), it is tempting to speculate that FST secretion by cancer cells might block an essential signal required to coordinate innate and adaptive immune response against the tumor. These data suggest FST could represent a novel predictive biomarker of sensitivity to ICB blockade and a therapeutic target whose inhibition could sensitize HGSC to immunotherapy (70, 71).

In conclusion, our study highlights the unrealized potential of tumor genotype-driven strategies for optimizing protocols using combination checkpoint immunotherapy. The present proof-of-concept studies validate the use of novel syngeneic preclinical immunocompetent mouse models as experimental systems to explore tumor heterogeneity and treatment modalities of HGSCs.

METHODS

Cell Lines and Cell Culture

Fallopian tube cells were isolated from *Trp53*$^{flox/flox}$ (The Jackson Laboratory) and *Brca1*$^{flox/flox}$*Trp53*$^{flox/flox}$ (20) C57BL/6 mice female mice. The *Trp53*$^{flox/flox}$ and *Brca1*$^{flox/flox}$*Trp53*$^{flox/flox}$ fallopian tube organoids were generated as described previously (72). To deplete *Trp53* and *Brca1, Trp53*$^{flox/flox}$ and *Brca1*$^{flox/flox}$*Trp53*$^{flox/flox}$ fallopian tube organoids were dissociated into single cells and then infected with 10^5 pfu Adenovirus-CMV-Cre (Vector Development Lab, Baylor College of Medicine) and confirmed as previously described (73). The *Trp53*$^{-/-}$ and *Trp53*$^{-/-}$ *Brca1*$^{-/-}$ fallopian tube cells were released from the Matrigel (Corning Matrigel matrix, 47743-710) and single-cell sorted to introduce genetic alterations using lentiviral gene transduction (for mutations and overexpression) and CRISPR/Cas9 (for deletions) methodology as described in Fig. 1A and B. All cell lines were cultured in fallopian tube cells media (FT-media); DMEM supplemented with 1% insulin–transferrin–selenium (Thermo Fisher Scientific; ITS-G, 41400045), EGF (2 ng/mL), 4% heat-inactivated fetal bovine serum (Thermo Fisher Scientific; IFS, F4135), and 1% penicillin and streptomycin. All cultures were checked for *Mycoplasma* using the MycoAlert Plus Mycoplasma Detection Kits assay (Lonza LT07).

Site-specific point mutations were introduced using the NEB *Q5* Site-Directed Mutagenesis Kit on mouse *Trp53* plasmid (Addgene plasmid #22725) to generate mouse *Trp53*^{R172H} expressing plasmid. Subsequently, mutant mouse *Trp53*^{R172H} was cloned into pLV-EF1a-IRES-Hygro (Addgene plasmid #85134). Mouse *Ccne1* (Sino biological, MG50896-ACG) was cloned into pLV-EF1a-IRES-Neo (Addgene plasmid #85139). Mouse *Akt2* (Addgene plasmid #64832) was cloned into pLV-EF1a-IRES-Blast (Addgene plasmid #85133). For *Myc* overexpression, we used MSCV-Myc-PGK-Puro-IRES-GFP (Addgene plasmid #75124), and for *KRAS*^{G12V}, we used pUG2K (Addgene plasmid #35493). The lentiviral vector used to overexpress *Brd4-short isoform, Smarca4*, and *Fst* in our study, pLV[Exp]-EF1A>mBrd4[NM_198094.2](ns):P2A:EGF and pLV[Exp]-EF1A>mSmarca4[NM_001357764.1](ns):P2A:EGFP and pLV[Exp]-mCherry-EF1A>mFst[NM_001301373.1] (VB200220-1171ukt) overexpression plasmids were used that were constructed by VectorBuilder. The vector ID was VB191212-2643ptd, VB191205-1922bak, and VB200220-1171ukt, which can be used to retrieve detailed information about the vector on www.vectorbuilder.com. Lentivirus-based constructs were packaged with the pMD2.G (VSVG; Addgene plasmid #12259) and psPAX2 plasmids (Addgene plasmid #12260). Retrovirus-based constructs were packaged with the pUMVC (Addgene plasmid #8449) and pMD2.G (VSVG; Addgene plasmid #12259). Viral infections were performed using 10 μg/mL polybrene transfection reagent (Thermo Fisher Scientific; TR1003G) for eight hours. After viral transduction, selection was performed using Hygromycin B (Life Technologies 10687010), neomycin-Geneticin Selective Antibiotic (G418 Sulfate, Life Technologies 11811031), and Blasticidin S HCl (Life Technologies R21001). Genetic alterations using lentiviral gene transduction (for mutations and overexpression) and CRISPR/Cas9 (for deletions) were confirmed by PCR-based analysis and immunoblotting. For PCR-based verification of *KRAS*^{G12V}, mutant *Trp53*^{R172H}, and *Brca1*, the primers are listed in Supplementary Material and Methods Table S1. Briefly, the genomic DNA was extracted from cells using the Purelink Genomic DNA Mini Kit (Life Technologies, K182001), following the manufacturer's instructions. Subsequently, 2X Q5 High-Fidelity Polymerase (New England Biolabs, M0494L) in Nuclease-free (Life Technologies, AM9937) was used to amplify the locus of interest using the manufacturer's instructions. PCR products were separated on 1% agarose gel; see Supplementary Material and Methods Table S1 for primer sequences for PCR. For induction of p21 in a p53-dependent manner, we treated the m-FTE cell lines and mouse embryonic fibroblasts (ATCC SCRC-1040) with or without Nocodazole (0.125 μg/mL; ref. 74; Selleckchem, S2775) for 24 hours.

CRISPR/Cas9 Targeting and Confirmation Using Sanger Sequencing of Modified Loci

Murine CRISPR/Cas9-GFP–expressing knockout plasmids were obtained from Santa Cruz Biotechnology. For *Pten* (SC-422475), *Nf1* (SC-421861), *S100a4* (SC-422782), *Fst* (SC-420417), and *Il33* (SC-429508): Briefly, 0.5×10^6 cells/well were seeded into a 6-well tissue culture plate and incubated overnight. CRISPR/Cas9 KO plasmids were transfected according to the manufacturer's instructions. For isolation of Cas9-GFP–expressing cell populations, cells were

sorted by flow cytometry (sorted for GFP-positive cells) and seeded as single cells into 96-well flat-bottom plates (Westnet Inc., 3595). The single guide RNA (sgRNA) sequences are listed in Supplementary Material and Methods Table S2.

Confirmation of clonal expanded CRISPR/Cas9 knockout cell lines was performed by Sanger DNA sequencing. Genomic DNA was extracted from cells using the Purelink Genomic DNA Mini Kit (Life Technologies, K182001), following the manufacturer's instructions. Next, the deleted DNA regions were PCR amplified. The respective locus (<1,000 ng) was amplified using primers (0.5 μmol/L) spanning potential sites of deletion with 2X Q5 High-Fidelity Polymerase (New England Biolabs, M0494L) in nuclease-free buffer (Life Technologies, AM9937), following the manufacturer's instructions. PCR products were separated on 1% agarose gel. DNA fragments were excised from the agarose gel, and DNA was gel purified using the Zymoclean Gel DNA Recovery Kit (Zymo Research, 77001-146), following the manufacturer's instructions. Next, PCR products of the *PTEN* and *NF1* genomic regions were cloned using the CloneJET PCR Cloning Kit (Life Technologies, K123240). Transformation products were spread on LB Agar Carbenicillin plates and incubated overnight at 37°C. Colonies were sequenced, and data were analyzed using SnapGene 5.1 (BioTech), in which reads were mapped to the reference sequences. See Supplementary Material and Methods Table S2 for CRISPR/Cas9 plasmids and sgRNA sequences for CRISPR/Cas9 targeting and confirmation using Sanger sequencing of modified loci.

Animal Experiments

For animal studies, C57BL/6 mice (Jackson Laboratory, stock #000664) were used. Before injection, three million cells were suspended in Matrigel (Corning Matrigel matrix, 47743-710):FT-media (1:1). The cell mix with Matrigel was administered intraperitoneally into 8–12-week-old female mice. Tumor burden was monitored using 2D *in vivo* imaging system (IVIS) bioluminescence imaging. Briefly, the mice were injected with 150 mg/kg D-luciferin Firefly (PerkinElmer, 122799), and luminescence was assessed 15 minutes later using the Xenogen IVIS-100 Imaging System. Images were analyzed with Living Image Software 4.7.3. As per the indicated treatment strategy, mice were injected intraperitoneally with the indicated doses. Carboplatin (Patterson Veterinary Supply, 07-890-7778; dose, 30 mg/kg), olaparib (Selleckchem, S1060; dose, 50 mg/kg; ref. 75), and prexasertib (Selleckchem, S7178; dose, 10 mg/kg) were used. Olaparib and prexasertib were resuspended for *in vivo* injections according to the manufacturers' instructions. For immunotherapy, anti-CTLA4 (dose, 50 μg; Bio X Cell, BE0131) and anti–PD-L1 (dose, 50 μg; Bio X Cell, BE0101), respectively, were used. Treatments were repeated twice a week for a total of four weeks. Control mice were injected with either saline or 4% DMSO or isotype control antibody. *In vivo* depletion of $CD8^+$ T cells was achieved by intraperitoneal injection of 200 μg per mouse YST-169.4 (anti-CD8) monoclonal antibody (Bio X Cell). The treatment regimen is illustrated in Fig. 5G. One weekly dose was administered intraperitoneally for four weeks, and mice were monitored for survival. T-cell depletion experiment was repeated independently two times with three to four mice per group. For the rechallenge experiment, one million KPCA cells/mouse were injected intraperitoneally, as described earlier. The MIT Committee on Animal Care approved all animal study protocols. All cell lines were murine pathogen tested and confirmed *Mycoplasma* negative using MycoAlert Plus Mycoplasma Detection Kit assay (Lonza LT07).

Western Blot

For protein isolation, cells were washed twice with ice-cold PBS and placed on ice. Cells were lysed with the RIPA Buffer (Sigma-Aldrich, R0278) supplemented with a protease inhibitor (Sigma-Aldrich, 11873580001) and a phosphatase inhibitor (Roche Diagnostics, 4906845001) on ice and then flash-frozen on dry ice. Before analysis, lysates were spun down at 15,000 × *g* for 15 minutes at 4°C, and the supernatants were used for all subsequent procedures. Proteins with low concentration were filtered by Amicon Ultra-0.5 mL centrifugal filters (Millipore, UFC500396). The protein concentration was analyzed by the DC Protein Assay Kit (Bio-Rad, DC Protein Assay Kit II, 5000112) according to the manufacturer's instructions. Cell lysates (25 μg) were loaded to NuPAGE Novec 4%–12% Bis-Tris gels (Thermo Fisher Scientific) and then transferred to nitrocellulose membrane (Thermo Fisher Scientific) by electroblotting following the manufacturer's recommendations. Membranes were blocked using 5% nonfat milk in 1X Tris-buffered Saline, 0.1% Tween 20 (TBST) for 1 hour, and subsequently washed twice in 0.1% TBST. Primary antibody dilutions were used as mentioned in the antibodies listed in Supplementary Material and Methods Table S3 and incubated overnight at 4°C. Blots were washed, and the secondary antibody was used at 1:2,000 dilution. Antigen detection was done by luminol-based enhanced using Western Lightning Plus-ECL, Enhanced Chemiluminescence Substrate (PerkinElmer, NEL104001EA), and exposed to X-ray film (Thermo Fisher Scientific, PI34091). See Supplementary Material and Methods Table S3 for antibodies used.

Immunofluorescence

Engineered m-FTE cells (0.03×10^6 cells/well) were seeded to Nunc Lab-Tek II CC2 8-well Chamber Slides (Life Technologies, 154941). After 24 hours, cells were fixed with 4% paraformaldehyde (PFA; Life Technologies, 28906) for 10 minutes and then permeabilized with 0.2% Triton X-100 in PBS for 5 minutes. Blocking was done with 5% bovine serum albumin (Sigma, A2153) in PBS for 1 hour, and then cells were incubated with various primary antibodies (Supplementary Material and Methods Table S3) for 1.5 hours at room temperature. After that, secondary antibodies (1:500; Biotum) were used according to the primary antibody species. The cells were incubated with secondary antibody diluted in blocking buffer for 1 hour and washed with PBS. For nuclear staining, cells were incubated with DAPI (1:1,000; Life Technologies, 62248) for 5 minutes. The cells were washed twice with PBS and mounted with Prolong Gold antifade reagent (Life Technologies, P36930). Slides were covered and stored in the dark at 4°C. Subsequently, images were acquired at 63× magnification by using a Zeiss inverted microscope. Zen Lite Digital Imaging (AxioVision, Zeiss) software platform was used for the image processing and analyses. See Supplementary Material and Methods Table S3 for antibodies used.

IR-Induced RAD51 Foci

Engineered m-FTE cells were irradiated with a 10-Gy dose of IR and then fixed 6 hours after IR. Cells were washed with CSK buffer (100 mmol/L NaCl, 300 mmol/L sucrose, 10 mmol/L PIPES pH 7.0, 3 mmol/L MgCl2) and permeabilized with 0.2% Triton X-100 in CSK buffer for 2.5 minutes. Cells were washed in PBS and then fixed cells with 4% PFA, washed twice with PBS and blocked with 5% BSA in PBS for 15 minutes at room temperature. Cells were incubated with primary antibody RAD51 (Santa Cruz; SC-8349; 1:150) and g-H2AX (Millipore; 05-636; 1:5,000) 5% BSA for 35 minutes at 37°C followed by incubation of secondary antibodies in 1% PBS for 25 minutes at 37°C. Cells were mounted with DAPI, and images were acquired with an Axiocam 506 camera, controlled by Zen software. The RAD51 foci were quantified with CellProfiler image analysis software.

Cell Cytotoxicity Assay

In vitro cell cytotoxicity assays were performed with CellTiter-Glo Luminescent Cell Viability Assay (Promega), according to the manufacturer's instructions. Cells were seeded to opaque-walled

black clear-bottom 96-well plates (Thermo Fisher Scientific) and incubated overnight. The next day, indicated concentrations of the drugs being tested were added: carboplatin (Patterson Veterinary Supply, 07-890-7778), cisplatin (Patterson Veterinary Supply, 07-893-4099), prexasertib (Selleckchem, S71178), olaparib (Selleckchem, S1060), niraparib (Selleckchem, S7625), OTX015 (MK 8628/birabresib; Selleckchem, S7360), CPI-203 (Selleckchem, S7304), and (+)–JQ1, a BET bromodomain inhibitor (Abcam, ab146612), for 72 hours. For synergy analysis of prexasertib and olaparib treatment (Fig. 4A and B), cells were plated as above. The Bliss synergy score was calculated using SynergyFinder, a web application for analyzing drug combination dose–response matrix data (76). Luminescent Cell Viability Assay using CellTiter-Glo (Promega, G7571) was performed as per the manufacturer's instructions. IC_{50} values were determined using GraphPad Prism 8 (see Supplementary Table S1).

IHC

Omental tumor tissues were fixed with 10% neutral buffered formalin (Sigma-Aldrich, HT501128) overnight. The fixed samples were passed through the alcohol series, cleared with xylene, and embedded in paraffin blocks. Subsequently, 5-μm-thick sections were cut from the paraffin-embedded blocks. First, for IHC analyses, slides were dewaxed at 60°C for 20 minutes and rehydrated with the following graded ethanol washing steps. After antigen retrieval (with either citrate buffer or HIER buffer according to the antibody) in a pressure cooker, blocking was done with PBS with 0.3% TritonX-100 + 1% donkey serum for 20 minutes. After blocking, sections were incubated with various antibodies overnight at 4°C. The next day, slides were washed with PBS, and VECTASTAIN Elite ABC Kits (Vector Laboratories) was used for secondary antibody according to the manufacturers' instructions. Staining was developed with the IMMPACT DAB HRP substrate kit (Vector Laboratories, SK-4105), and counterstaining was done with hematoxylin. Slides were mounted, and whole slide scanned (20× magnification) at the Histology Core Facility, Koch Institute for Integrative Cancer Research at MIT; see Supplementary Material and Methods Table S3 for the antibodies used.

Tissue Processing

Omental tumors were collected and digested with collagenase (Sigma-Aldrich; 11088793001), hyaluronidase (Sigma-Aldrich, H3506), and DNAase (Sigma-Aldrich) at 37°C for 45 minutes. The single-cell suspension was obtained by passage through a 70-μm filter (Westnet Inc., 35235) and several washing steps with PBS. Pellet was resuspended with ACK lysis buffer (Life Technologies, A1049201) to lyse red blood cells at room temperature for 10 minutes and washed with PBS. Ascites were harvested, spun down at 1,000 × *g* for 10 minutes at 4°C, and the supernatants were stored for cytokine analysis. The pellet was lysed with ACK lysis buffer to lyse red blood cells at room temperature for 10 minutes and washed with PBS. After obtaining single-cell suspensions, cells were counted and then used for scRNA-seq and multiparameter flow cytometry analyses. For scRNA-seq, whole omental tumors (pooled four omental tumors/genotype) at the terminal time point of tumor growth from mice were implanted with either the BPPNM, PPNM, KPCA, or KPCA.C cells for analysis.

Single-Cell RNA-seq

Cell Ranger (version 3.0.2) using standard parameters was used, and samples were aligned against the refdata-cell ranger-mm10-1.2.0 reference sequences. For details about the samples, please see Supplementary Table S3. Samples were analyzed using Seurat 3.1.0. Samples were filtered for mitochondrial percentage <20% and merged based on the Seurat "Integration and Label Transfer" vignette using 3,000 integration features while keeping all shared genes for further analysis. Standard parameters for visualization and clustering were used throughout the analysis. Clusters were identified based on marker genes and subsequently joined into larger groups (Supplementary Tables S3–S5).

Multiparameter Flow Cytometry

Cells were plated to a 96-well V-bottom plate (Westnet Inc., 3894) and incubated with Zombie NIR Fixable Viability Kit (BioLegend, 423105) for 15 minutes at room temperature. The cells were washed with the staining buffer (PBS + 1% BSA + 0.1% sodium azide) and then blocked with anti-mouse CD16/32 (BioLegend, 101302) in staining buffer for 10 minutes on ice. Cells were incubated with primary antibodies for 30 minutes on ice and then washed with staining buffer. The antibody panels and the list of the antibodies are listed in Supplementary Material and Methods Tables S4 and S5. Detection of intracellular markers was carried out using the FoxP3 intracellular staining kit (Thermo 00-5523-00) following the manufacturer's protocol. Immunostained cells were run on an LSRFortessa HTS or LSRFortessa with FACSDiva software and analyzed using FlowJo V10.5.3. See Supplementary Material and Methods Tables S4 and S5 for the antibody panels used for multiparameter flow cytometry.

RNA-seq

For bulk-tumor RNA-seq, omental tumors were harvested and then flash-frozen in liquid nitrogen. For total RNA extraction, the *mir*Vana miRNA Isolation Kit, with phenol (Thermo Fisher Scientific, AM1560), was used according to the manufacturer's instructions. For RNA extraction from cell lines, cells were lysed with QIAzol lysis reagent and then flash-frozen in liquid nitrogen. For total RNA extraction, the miRNeasy RNA extraction kit (Thermo Fisher Scientific, 217004) was used according to the manufacturer's instructions. All the samples in this study were sent to BPF Next-Gen Sequencing Core Facility at Harvard Medical School for RNA-seq.

For RNA-seq analysis—mapping, differential expression, and gene enrichment analysis—the 75-nt long reads were mapped with STAR 2.7.1 (77) to the mm10 version of the mouse genome using the "sjdbOverhang" parameter set to 74, an annotation file from ENSEMBL version GRCm38.97 and the "alignIntronMax" parameter set to 50,000. We had between 9 and 17 million reads per sample and mapped between 7.5 and 14 million reads per sample.

The number of counts per gene was obtained using featureCounts (78) with the "-s" parameter set to 2, the same annotation file used for mapping, and the rest of the parameters left as the default option. Normalization and differential expression were done with DESeq2 (79); the genes with zero counts were removed in all samples. We converted mouse symbols to human symbols using orthologs from ENSEMBL. After that, we had between 14,000 and 15,000 genes that we ranked by fold changes and used as input into the GseaPreranked tool from the Broad Institute (48). We ran the GseaPreranked tool using the hallmark annotation "h.all.v7.1.symbols.gmt" and the GO annotation "c5.all.v7.1.symbols.gmt" files downloaded from the Broad Institute. Dot plots of the enrichment analysis were done using a custom R script and the GseaPreranked tool's outputs.

In Situ *Hybridization*

The RNAscope 2.5 HD Detection Kit (Advanced Cell Diagnostics, ACD) was used for the *in situ* hybridization of FST (RNAscope Probe no. Mm-Fst-454331) according to the manufacturer's instructions for formalin-fixed paraffin-embedded tissue sections. The fixed omental samples were briefly passed through the alcohol series, cleared with xylene, and embedded in paraffin blocks. Subsequently, 5-μm-thick sections were cut from the paraffin-embedded

blocks. RNAscope 2.5 HD Detection Reagent—RED (ACD, 322360) Kit, along with assay controls RNAscope Probe—Mm-Ppib (ACD, 313911) and RNAscope Probe—DapB (ACD, 310043), were used according to the manufacturer's instructions. After the staining, slides were mounted and whole-slide scanned (20× magnification) at the Histology Core Facility, Koch Institute for Integrative Cancer Research at MIT.

Cytokine and Chemokine Analysis

The Mouse Cytokine Array/Chemokine Array 44-Plex (MD44) and Cytokine Array, TGFβ 3-Plex (Multispecies; TGFB1-3) were used at the recommended dilutions. For HGSC mouse models, cytokine and chemokine analyses were performed from both cell culture and ascite supernatant samples. For the analysis of cytokine and chemokine on cell culture supernatants, cells were seeded to a 12-well tissue culture plate and were allowed to adhere overnight. The next day, the cells were washed twice with PBS and then replenished with serum-free DME plus 1% penicillin/streptomycin media. After 24 hours, cell culture supernatants were collected on ice and then flash-frozen on dry ice. Ascites and cell culture supernatants were profiled for cytokines and chemokines using services at Eve Technologies.

For mouse cytokine/chemokine analysis, the intensity measurements out of the observed range in >60% of the samples were removed from the analysis (TIMP, IL16, and CCL21, 6Ckine/Exodus 2). Concentrations corresponding to intensity values out of range were imputed with the most extreme value from the expected concentration in the standard curve for each cytokine. Samples were grouped based on the genotype and subjected to the nonparametric Mann–Whitney test to identify differentially expressed cytokines between the two groups, and visualized using *z*-score column normalization and hierarchical clustering.

The Human Cytokine/Chemokine 65-Plex Panel (HD65) and TGFβ3-Plex (Multispecies) Cytokine Array (TGFB1-3) were used at the recommended dilutions. Cytokines out of the observed range intensity measurements in >60% of the samples were removed from the analysis (TIMP, IL16, and 6Ckine/Exodus 2). Concentrations corresponding to intensity values out of range were imputed with the most extreme value from the expected concentration in the standard curve for each cytokine. Outliers in the human samples were detected with multidimensional scaling and removed (ascites and serum 2, 5, 10, and 14). Samples were grouped into HR-proficient and HR-deficient based on the genotype and subjected to the nonparametric Mann–Whitney test to identify differentially expressed cytokines between them. Patient ascite supernatants were profiled for cytokines and chemokines using services at Eve Technologies. Patients gave their written informed consent to participate in the Hercules study. The study was conducted in accordance with the Declaration of Helsinki and approved by The Ethics Committee of the Hospital District of Southwest Finland, decision: ETMK Dnro: 145/1801/2015.

An ELISA was used to measure the levels of FST in cell culture supernatants. Mouse FST ELISA Kit (Ray Biotech, ELM-FST-1) was used according to the manufacturer's instructions. Briefly, cells were seeded to a 12-well tissue culture plate and allowed to adhere overnight. The next day, the cells were washed twice with PBS and then replenished and stimulated with serum-free DME plus the stimulants or unstimulated (as a control group) for ELISA. For FST ELISA assay, TGFβ (R&D Systems, 240-B-002) was added as the stimulant for 24 hours before the collection of the supernatant. Absorbances were measured according to the manufacturer's instructions. GraphPad Prism 8 was used for analysis.

Chemotaxis Cell Migration Assay

To examine tumor-infiltrating immune cell migration, we used *in vitro* Transwell chemotaxis assay (QCM Chemotaxis Cell Migration Assay, 24-well (5 μm) and Fluorimetric Activity Assay (MilliporeSigma, ECM507). Briefly, we collected cell culture supernatants (as described above) from BPPNM and KPCA cells and freshly isolated purified $CD45^+$ cells (CD45, TIL) using mouse-specific MicroBeads (Miltenyi Biotec, 130-110-618) from BPPNM and KPCA tumors (Supplementary Fig. S4E). Purified $CD45^+$ cells (CD45 Microbeads, mouse; Miltenyi Biotec, 130-097-153) were used to control/check purity of sorted $CD45^+$ cells (Supplementary Fig. S4E). Freshly purified bulk $CD45^+$ cells from BPPNM or KPCA tumors were placed in the Transwell chamber's top well. Supernatants from BPPNM or KPCA cells were placed in the lower chamber with or without appropriate neutralizing antibodies (Mouse GM-CSF Antibody; 0.3 μg/mL; R&D Systems, MAB415) and TGFβ 1,2,3 (3 μg/mL; R&D Systems, MAB1835). The Transwell plates were incubated for 16–18 hours at 37°C under a 5% CO_2 atmosphere. The inserts were removed, and cells that had migrated to each bottom well were collected and then incubated with primary antibodies (cell-surface antibodies) for 30 minutes on ice and then washed with staining buffer with DAPI (for Live/Dead staining). The antibody panels and the list of the antibodies are given in Supplementary Material and Methods Tables S4 and S5. Immunostained cells were run on an LSRFortessa with FACSDiva software and analyzed using FlowJo V10.5.3. Each antibody and controls were tested in triplicate. The data presented are pooled from two independent experiments. See Supplementary Material and Methods Tables S4 and S5 for the antibody panels used for multiparameter flow cytometry.

Whole-Exome Sequencing

DNA was extracted from cells using the Purelink Genomic DNA Mini Kit (Life Technologies, K182001), following the manufacturer's instructions. The samples were sent to the Beijing Genomics Institute (BGI) for DNBseq WES. Exome reads were filtered to remove low-quality reads and then mapped to the mouse genome (mm10) using bwa mem (version 0.7.15). Multimapped reads were removed, producing 190-fold coverage across targeted regions. Single-nucleotide variants (SNV) were identified in both samples using GATK's HaplotypeCaller. SNVs were filtered with GATK (using –filterExpression "QD<2.0 || FS>60 || MQ<40 || MQRankSum←12.5 || ReadPosRankSum←8.0"). SNV positions were further characterized using bam-readcount (version 0.7.4) by counting reads supporting each allele at each position. The overall most prevalent variant at each SNV position was determined, and the fraction of reads supporting that allele was calculated for each sample. After adding 0.1 to each fraction (to avoid division by 0), these allele fractions were compared at each SNV position. Furthermore, to identify variants, positions with coverage of at least 50 reads and at least a 2-fold difference between samples were highlighted in blue.

Analysis of Copy-Number Alterations and HRD-LOH Score

DNA was extracted from cells using the Purelink Genomic DNA Mini kit (Life Technologies, K182001), following the manufacturer's instructions. The samples were sent to NYU Langone's Genome Technology Center for low-pass WGS. Paired reads from WGS were mapped to the mouse genome (mm10) using bwa mem (version 0.7.15) with default settings. After removing any mappings to chrM or chrY, read-depth variations and CNAs were identified using the program Control-FREEC (24) v11.6 using SNPs from ENSEMBL Release 101, a GEM mappability file, and the following settings: window = 50000, breakPointThreshold = 0.6, minimalCoveragePerPosition = 1, minimalQualityPerPosition = 5, ploidy = 2, sex = XX, and shiftInQuality = 33. CNAs with a high level of uncertainty (>95 percentage) were ignored. The LOH events > 15MB (25) were identified using the program scarHRD (26).

ATAC-seq Analysis

Cells were harvested and frozen in culture media containing FBS and 5% DMSO. Cryopreserved cells were sent to Active Motif

to perform the ATAC-seq assay. The cells were then thawed in a 37°C water bath, pelleted, washed with cold PBS, and tagmented as previously described (80), with some modifications based on ref. 81. Briefly, cell pellets were resuspended in lysis buffer, pelleted, and tagmented using the enzyme and buffer provided in the Nextera Library Prep Kit (Illumina). Tagmented DNA was then purified using the MinElute PCR purification kit (Qiagen), amplified with 10 cycles of PCR, and purified using Agencourt AMPure SPRI beads (Beckman Coulter). The resulting material was quantified using the KAPA Library Quantification Kit for Illumina platforms (KAPA Biosystems) and sequenced with PE42 sequencing on the NextSeq 500 sequencer (Illumina).

Paired-end reads were filtered to remove low-quality reads and then mapped to the mouse genome (mm10) using bwa mem (version 0.7.12), and peaks were called with MACS v2.1.0. Peaks were merged across samples, and read coverage of each peak was determined with "bedtools coverage." For each FST peak, chromatin accessibility was compared between samples with Fisher exact test, using contingency tables of read counts for one peak and for all peaks on that chromosome. The *P* values were FDR corrected. For the combined FST peaks, chromatin accessibility was compared similarly, using contingency tables of read counts across four peaks and for all peaks on that chromosome.

TCGA Ovarian Cancer Survival Analysis

Using genomic and transcriptomic data from the TCGA, we identified 78 patients with *BRCA1/2* deficiency as defined by *BRCA1/2* somatic or germline mutation or hypermethylation, and 72 patients with *CCNE1*-amplified tumors with corresponding transcriptomic gene-expression and survival data. The *FST* mRNA expression levels were normalized for fragments per kilobase million, log-transformed, and divided into high and low based on the median expression. The difference between the PFS as the time from diagnosis to recurrence, or overall survival as the time from diagnosis to death, was evaluated with the Kaplan–Meier method using the log-rank test or Cox regression analysis. The results shown here are in whole or part based upon data generated by the TCGA Research Network: https://www.cancer.gov/tcga.

Statistical Analysis

Statistical analysis was performed using GraphPad Prism 8 software (GraphPad Software, Inc.), using an independent sample *t* test unless otherwise indicated. $P \leq 0.05$ was considered as significant. Data are represented as mean ± standard error of the mean (SEM). The log-rank (Mantel–Cox) test was used to analyze the survival difference in the treatment and the untreated-matched cohorts.

Data Availability

scRNA-seq, bulk RNA-seq, WGS, and WES data have been deposited in the Gene Expression Omnibus database under the accession code GSE158474. All other data supporting this study's findings are available within the article or the Supplementary information files, or from the corresponding author upon request.

Authors' Disclosures

S. Iyer reports a patent pending. J. Oikkonen reports grants from European Union's Horizon 2020 research and innovation program and grants from Sigrid Jusélius Foundation during the conduct of the study. B.G. Neel reports grants from Mary Kay Foundation during the conduct of the study; personal fees from Drinker-Biddle, personal fees and other from Northern Biologics, Arvinas, Inc, and Navire Pharma, other from Amgen, Inc, Regeneron, Inc, Moderna, Inc, and Gilead, Inc outside the submitted work. D. Pépin reports grants from Koch Institute for Integrative Cancer Research at MIT during the conduct of the study; in addition, Dr. Pépin has a patent for treatment selection and assessment of therapeutic response in FST-secreting cancers pending. R.A. Weinberg is a shareholder in Verastem Inc and on its Board of Scientific Advisors. No disclosures were reported by the other authors.

Authors' Contributions

S. Iyer: Conceptualization, resources, data curation, formal analysis, supervision, funding acquisition, validation, investigation, visualization, methodology, writing–original draft, project administration, writing–review and editing. **S. Zhang:** Resources, writing–review and editing. **S. Yucel:** Data curation, software, formal analysis, validation, visualization, methodology, writing–review and editing. **H. Horn:** Data curation, software, formal analysis, validation, visualization, methodology, writing–review and editing. **S.G. Smith:** Data curation, formal analysis, validation, visualization, methodology, writing–review and editing. **F. Reinhardt:** Data curation, formal analysis, and validation. **E. Hoefsmit:** Data curation, formal analysis, writing–review and editing. **B. Assatova:** Data curation. **J. Casado:** Software, formal analysis, validation, and methodology. **M.-C. Meinsohn:** Data curation and formal analysis. **M.I. Barrasa:** Software, formal analysis, validation, and methodology. **G.W. Bell:** Software, formal analysis, and methodology. **F. Perez-Villatoro:** Resources, software, formal analysis, and methodology. **K. Huhtinen:** Resources and supervision. **J. Hynninen:** Resources, writing–review and editing. **J. Oikkonen:** Resources, data curation, formal analysis, methodology, writing–review and editing. **P.M. Galhenage:** Formal analysis, visualization, methodology. **S. Pathania:** Formal analysis, visualization, methodology, supervision. **P.T. Hammond:** Formal analysis and supervision. **B.G. Neel:** Resources, writing–review and editing. **A. Farkkila:** Resources, data curation, software, formal analysis, methodology, writing–review and editing. **D. Pépin:** conceptualization, resources, data curation, software, formal analysis, supervision, funding acquisition, validation, investigation, methodology, writing–review and editing. **R.A. Weinberg:** Conceptualization, resources, supervision, funding acquisition, writing–original draft, writing–review and editing.

Acknowledgments

We would like to thank the Weinberg lab members, Richard Goldsby, Heather R. Keys, Tsukasa Shibue, Ellen Duong, and Kevin M. Elias, for essential comments and suggestions during this work. We would also like to thank Yeku Oladapo and Patricia K. Donahoe for their comments on the manuscript. We would like to thank Duygu Hatice Saatcioglu and Raghav Mohan for assistance in processing tissues for scRNA-seq. We would like to thank Dong Dong, Tian Xia, Omer Faruk Karakaya, and Tony E Chavarria for assistance in processing tumor tissues. We would like to thank Sunny Das for help in the synergy analysis. We would like to thank Roderick T. Bronson for assistance in the histopathologic examination of the tumors. The cartoons were created with BioRender.com. We would like to thank the Flow Cytometry Core Facility at the Whitehead Institute for Biomedical Research. We would like to thank the Hope Babette Tang Histology Facility, Swanson Biotechnology Center Flow Cytometry Core, and High Throughput Sciences Core Facilities at Koch Institute for Integrative Cancer Research at MIT. We thank BPF Next-Gen Sequencing Core Facility at Harvard Medical School for RNA-seq. We thank the NYU Langone's Genome Technology Center for WGS. We thank the Active Motif for the ATAC-seq assay. We thank the BGI for WES. We thank Eve Technologies (Calgary, Canada) services for cytokines and chemokines. S. Iyer was supported by the postdoctoral fellowship by Ludwig Fund for Cancer Research and Amgen. R.A. Weinberg was funded by grants from the NIH (R01 CA0784561 and P01

CA080111), Nancy Peery Marriott Foundation, Samuel Waxman Cancer Research Foundation, Breast Cancer Research Foundation, and Ludwig Fund for Cancer Research. This work was supported by the Bridge Project, a partnership between the Koch Institute for Integrative Cancer Research at MIT and the Dana-Farber/Harvard Cancer Center. D. Pépin was supported by the Assistant Secretary of Defense for Health Affairs through the Ovarian Cancer Research Program under Award No. W81XWH-17-1-0212. The US Army Medical Research Acquisition Activity, 820 Chandler Street, Fort Detrick MD 21702-5014 is the awarding and administering acquisition office. Opinions, interpretations, conclusions, and recommendations are those of the authors and are not necessarily endorsed by the Department of Defense. In conducting research using animals, the investigator(s) adheres to the laws of the United States and regulations of the Department of Agriculture. This project has been supported by the European Union's Horizon 2020 research and innovation program under grant agreement No 667403 for HERCULES.

Received June 11, 2020; revised September 8, 2020; accepted November 3, 2020; published first November 6, 2020.

REFERENCES

1. The Cancer Genome Atlas Research Network. Integrated genomic analyses of ovarian carcinoma. Nature 2011;474:609–15.
2. Moore K, Colombo N, Scambia G, Kim BG, Oaknin A, Friedlander M, et al. Maintenance olaparib in patients with newly diagnosed advanced ovarian cancer. N Engl J Med 2018;379:2495–505.
3. Konstantinopoulos PA, Ceccaldi R, Shapiro GI, D'Andrea AD. Homologous recombination deficiency: exploiting the fundamental vulnerability of ovarian cancer. Cancer Discov 2015;5:1137–54.
4. Au-Yeung G, Lang F, Azar WJ, Mitchell C, Jarman KE, Lackovic K, et al. Selective targeting of cyclin E1-amplified high-grade serous ovarian cancer by cyclin-dependent kinase 2 and AKT inhibition. Clin Cancer Res 2017;23:1862–74.
5. Coukos G, Tanyi J, Kandalaft LE. Opportunities in immunotherapy of ovarian cancer. Ann Oncol 2016;27:i11–i5.
6. Ribas A, Wolchok JD. Cancer immunotherapy using checkpoint blockade. Science 2018;359:1350–5.
7. Matulonis UA, Shapira-Frommer R, Santin AD, Lisyanskaya AS, Pignata S, Vergote I, et al. Antitumor activity and safety of pembrolizumab in patients with advanced recurrent ovarian cancer: results from the phase II KEYNOTE-100 study. Ann Oncol 2019;30:1080–7.
8. Disis ML, Taylor MH, Kelly K, Beck JT, Gordon M, Moore KM, et al. Efficacy and safety of avelumab for patients with recurrent or refractory ovarian cancer: phase 1b results from the JAVELIN solid tumor trial. JAMA Oncol 2019;5:393–401.
9. Keenan TE, Burke KP, Van Allen EM. Genomic correlates of response to immune checkpoint blockade. Nat Med 2019;25:389–402.
10. Kuhn E, Tisato V, Rimondi E, Secchiero P. Current preclinical models of ovarian cancer. J Carcinog Mutagen 2015;6:220.
11. Roby KF, Taylor CC, Sweetwood JP, Cheng Y, Pace JL, Tawfik O, et al. Development of a syngeneic mouse model for events related to ovarian cancer. Carcinogenesis 2000;21:585–91.
12. Walton J, Blagih J, Ennis D, Leung E, Dowson S, Farquharson M, et al. CRISPR/Cas9-mediated Trp53 and Brca2 knockout to generate improved murine models of ovarian high-grade serous carcinoma. Cancer Res 2016;76:6118–29.
13. Janat-Amsbury MM, Yockman JW, Anderson ML, Kieback DG, Kim SW. Comparison of ID8 MOSE and VEGF-modified ID8 cell lines in an immunocompetent animal model for human ovarian cancer. Anticancer Res 2006;26:2785–9.
14. Stuckelberger S, Drapkin R. Precious GEMMs: emergence of faithful models for ovarian cancer research. J Pathol 2018;245:129–31.
15. Zhai Y, Wu R, Kuick R, Sessine MS, Schulman S, Green M, et al. High-grade serous carcinomas arise in the mouse oviduct via defects linked to the human disease. J Pathol 2017;243:16–25.
16. Kim J, Coffey DM, Creighton CJ, Yu Z, Hawkins SM, Matzuk MM. High-grade serous ovarian cancer arises from fallopian tube in a mouse model. Proc Natl Acad Sci U S A 2012;109:3921–6.
17. Perets R, Wyant GA, Muto KW, Bijron JG, Poole BB, Chin KT, et al. Transformation of the fallopian tube secretory epithelium leads to high-grade serous ovarian cancer in Brca;Tp53;Pten models. Cancer Cell 2013;24:751–65.
18. Karst AM, Levanon K, Drapkin R. Modeling high-grade serous ovarian carcinogenesis from the fallopian tube. Proc Natl Acad Sci U S A 2011;108:7547–52.
19. Crum CP, Drapkin R, Kindelberger D, Medeiros F, Miron A, Lee Y. Lessons from BRCA: the tubal fimbria emerges as an origin for pelvic serous cancer. Clin Med Res 2007;5:35–44.
20. Liu X, Holstege H, van der Gulden H, Treur-Mulder M, Zevenhoven J, Velds A, et al. Somatic loss of BRCA1 and p53 in mice induces mammary tumors with features of human BRCA1-mutated basal-like breast cancer. Proc Natl Acad Sci U S A 2007;104:12111–6.
21. Alamo P, Gallardo A, Di Nicolantonio F, Pavon MA, Casanova I, Trias M, et al. Higher metastatic efficiency of KRas G12V than KRas G13D in a colorectal cancer model. FASEB J 2015;29:464–76.
22. Qiu P, Shandilya H, D'Alessio JM, O'Connor K, Durocher J, Gerard GF. Mutation detection using surveyor nuclease. BioTechniques 2004;36:702–7.
23. Pao W, Wang TY, Riely GJ, Miller VA, Pan Q, Ladanyi M, et al. KRAS mutations and primary resistance of lung adenocarcinomas to gefitinib or erlotinib. PLoS Med 2005;2:e17.
24. Abkevich V, Timms KM, Hennessy BT, Potter J, Carey MS, Meyer LA, et al. Patterns of genomic loss of heterozygosity predict homologous recombination repair defects in epithelial ovarian cancer. Br J Cancer 2012;107:1776–82.
25. Boeva V, Popova T, Bleakley K, Chiche P, Cappo J, Schleiermacher G, et al. Control-FREEC: a tool for assessing copy number and allelic content using next-generation sequencing data. Bioinformatics 2012;28:423–5.
26. Sztupinszki Z, Diossy M, Krzystanek M, Reiniger L, Csabai I, Favero F, et al. Migrating the SNP array-based homologous recombination deficiency measures to next generation sequencing data of breast cancer. NPJ Breast Cancer 2018;4:16.
27. Mendes-Pereira AM, Martin SA, Brough R, McCarthy A, Taylor JR, Kim JS, et al. Synthetic lethal targeting of PTEN mutant cells with PARP inhibitors. EMBO Mol Med 2009;1:315–22.
28. Yin Y, Shen WH. PTEN: a new guardian of the genome. Oncogene 2008;27:5443–53.
29. Shen WH, Balajee AS, Wang J, Wu H, Eng C, Pandolfi PP, et al. Essential role for nuclear PTEN in maintaining chromosomal integrity. Cell 2007;128:157–70.
30. Qiu Z, Oleinick NL, Zhang J. ATR/CHK1 inhibitors and cancer therapy. Radiother Oncol 2018;126:450–64.
31. Lee JM, Nair J, Zimmer A, Lipkowitz S, Annunziata CM, Merino MJ, et al. Prexasertib, a cell cycle checkpoint kinase 1 and 2 inhibitor, in BRCA wild-type recurrent high-grade serous ovarian cancer: a first-in-class proof-of-concept phase 2 study. Lancet Oncol 2018;19:207–15.
32. Lengyel E. Ovarian cancer development and metastasis. Am J Pathol 2010;177:1053–64.
33. Bowtell DD, Bohm S, Ahmed AA, Aspuria PJ, Bast RC Jr., Beral V, et al. Rethinking ovarian cancer II: reducing mortality from high-grade serous ovarian cancer. Nat Rev Cancer 2015;15:668–79.
34. Klein AM, Mazutis L, Akartuna I, Tallapragada N, Veres A, Li V, et al. Droplet barcoding for single-cell transcriptomics applied to embryonic stem cells. Cell 2015;161:1187–201.
35. Broz ML, Binnewies M, Boldajipour B, Nelson AE, Pollack JL, Erle DJ, et al. Dissecting the tumor myeloid compartment reveals rare activating antigen-presenting cells critical for T cell immunity. Cancer Cell 2014;26:638–52.
36. Jiang Y, Li Y, Zhu B. T-cell exhaustion in the tumor microenvironment. Cell Death Dis 2015;6:e1792.

37. Wherry EJ. T cell exhaustion. Nat Immunol 2011;12:492–9.
38. Kumar V, Patel S, Tcyganov E, Gabrilovich DI. The nature of myeloid-derived suppressor cells in the tumor microenvironment. Trends Immunol 2016;37:208–20.
39. Giuntoli RL 2nd, Webb TJ, Zoso A, Rogers O, Diaz-Montes TP, Bristow RE, et al. Ovarian cancer-associated ascites demonstrates altered immune environment: implications for antitumor immunity. Anticancer Res 2009;29:2875–84.
40. Cardenas H, Jiang G, Thomes Pepin J, Parker JB, Condello S, Nephew KP, et al. Interferon-gamma signaling is associated with BRCA1 loss-of-function mutations in high grade serous ovarian cancer. NPJ Precis Oncol 2019;3:32.
41. Kipps E, Tan DS, Kaye SB. Meeting the challenge of ascites in ovarian cancer: new avenues for therapy and research. Nat Rev Cancer 2013;13:273–82.
42. Jimenez-Sanchez A, Memon D, Pourpe S, Veeraraghavan H, Li Y, Vargas HA, et al. Heterogeneous tumor-immune microenvironments among differentially growing metastases in an ovarian cancer patient. Cell 2017;170:927–38.
43. Jimenez-Sanchez A, Cybulska P, Mager KL, Koplev S, Cast O, Couturier DL, et al. Unraveling tumor-immune heterogeneity in advanced ovarian cancer uncovers immunogenic effect of chemotherapy. Nat Genet 2020;52:582–93.
44. Lee J, Ahn E, Kissick HT, Ahmed R. Reinvigorating exhausted T cells by blockade of the PD-1 pathway. For Immunopathol Dis Therap 2015;6:7–17.
45. Wherry EJ, Kurachi M. Molecular and cellular insights into T cell exhaustion. Nat Rev Immunol 2015;15:486–99.
46. Stewart RA, Pilie PG, Yap TA. Development of PARP and immune-checkpoint inhibitor combinations. Cancer Res 2018;78:6717–25.
47. Ding L, Kim HJ, Wang Q, Kearns M, Jiang T, Ohlson CE, et al. PARP inhibition elicits STING-dependent antitumor immunity in Brca1-deficient ovarian cancer. Cell Rep 2018;25:2972–80.
48. Subramanian A, Tamayo P, Mootha VK, Mukherjee S, Ebert BL, Gillette MA, et al. Gene set enrichment analysis: a knowledge-based approach for interpreting genome-wide expression profiles. Proc Natl Acad Sci U S A 2005;102:15545–50.
49. Farkkila A, Gulhan DC, Casado J, Jacobson CA, Nguyen H, Kochupurakkal B, et al. Immunogenomic profiling determines responses to combined PARP and PD-1 inhibition in ovarian cancer. Nat Commun 2020;11:1459.
50. Etemadmoghadam D, Weir BA, Au-Yeung G, Alsop K, Mitchell G, George J, et al. Synthetic lethality between CCNE1 amplification and loss of BRCA1. Proc Natl Acad Sci U S A 2013;110:19489–94.
51. Wei SC, Anang NAS, Sharma R, Andrews MC, Reuben A, Levine JH, et al. Combination anti-CTLA-4 plus anti-PD-1 checkpoint blockade utilizes cellular mechanisms partially distinct from monotherapies. Proc Natl Acad Sci U S A 2019;116:22699–709.
52. Sen T, Rodriguez BL, Chen L, Corte CMD, Morikawa N, Fujimoto J, et al. Targeting DNA damage response promotes antitumor immunity through STING-mediated T-cell activation in small cell lung cancer. Cancer Discov 2019;9:646–61.
53. Fazzini M, Vallejo G, Colman-Lerner A, Trigo R, Campo S, Baranao JL, et al. Transforming growth factor beta1 regulates follistatin mRNA expression during in vitro bovine granulosa cell differentiation. J Cell Physiol 2006;207:40–8.
54. Hedger MP, Winnall WR, Phillips DJ, de Kretser DM. The regulation and functions of activin and follistatin in inflammation and immunity. Vitam Horm 2011;85:255–97.
55. Kaneko H. Subchapter 33C—Follistatin. In: Takei Y, Ando H, Tsutsui K, editors. Handbook of hormones. San Diego: Academic Press; 2016. p. 298–e33C–2.
56. Ren P, Chen FF, Liu HY, Cui XL, Sun Y, Guan JL, et al. High serum levels of follistatin in patients with ovarian cancer. J Int Med Res 2012;40:877–86.
57. Antsiferova M, Werner S. The bright and the dark sides of activin in wound healing and cancer. J Cell Sci 2012;125:3929–37.
58. Morianos I, Papadopoulou G, Semitekolou M, Xanthou G. Activin-A in the regulation of immunity in health and disease. J Autoimmun 2019;104:102314.
59. Saatcioglu HD, Kano M, Horn H, Zhang L, Samore W, Nagykery N, et al. Single-cell sequencing of neonatal uterus reveals an Misr2+ endometrial progenitor indispensable for fertility. Elife 2019;8:e46349.
60. Yang L, Pang Y, Moses HL. TGF-beta and immune cells: an important regulatory axis in the tumor microenvironment and progression. Trends Immunol 2010;31:220–7.
61. Thomas DA, Massague J. TGF-beta directly targets cytotoxic T cell functions during tumor evasion of immune surveillance. Cancer Cell 2005;8:369–80.
62. Nagarsheth N, Wicha MS, Zou W. Chemokines in the cancer microenvironment and their relevance in cancer immunotherapy. Nat Rev Immunol 2017;17:559–72.
63. Strickland KC, Howitt BE, Shukla SA, Rodig S, Ritterhouse LL, Liu JF, et al. Association and prognostic significance of BRCA1/2-mutation status with neoantigen load, number of tumor-infiltrating lymphocytes and expression of PD-1/PD-L1 in high grade serous ovarian cancer. Oncotarget 2016;7:13587–98.
64. Emens LA, Middleton G. The interplay of immunotherapy and chemotherapy: harnessing potential synergies. Cancer Immunol Res 2015;3:436–43.
65. Kampan NC, Madondo MT, McNally OM, Stephens AN, Quinn MA, Plebanski M. Interleukin 6 present in inflammatory ascites from advanced epithelial ovarian cancer patients promotes tumor necrosis factor receptor 2-expressing regulatory T cells. Front Immunol 2017;8:1482.
66. Park MJ, Lee SH, Kim EK, Lee EJ, Baek JA, Park SH, et al. Interleukin-10 produced by myeloid-derived suppressor cells is critical for the induction of Tregs and attenuation of rheumatoid inflammation in mice. Sci Rep 2018;8:3753.
67. Vignali DA, Collison LW, Workman CJ. How regulatory T cells work. Nat Rev Immunol 2008;8:523–32.
68. Shi L, Resaul J, Owen S, Ye L, Jiang WG. Clinical and therapeutic implications of follistatin in solid tumours. Cancer Genomics Proteomics 2016;13:425–35.
69. Cash JN, Rejon CA, McPherron AC, Bernard DJ, Thompson TB. The structure of myostatin:follistatin 288: insights into receptor utilization and heparin binding. EMBO J 2009;28:2662–76.
70. Dreaden EC, Kong YW, Quadir MA, Correa S, Suarez-Lopez L, Barberio AE, et al. RNA-Peptide nanoplexes drug DNA damage pathways in high-grade serous ovarian tumors. Bioeng Transl Med 2018;3:26–36.
71. Gu L, Deng ZJ, Roy S, Hammond PT. A combination RNAi-chemotherapy layer-by-layer nanoparticle for systemic targeting of KRAS/P53 with cisplatin to treat non-small cell lung cancer. Clin Cancer Res 2017;23:7312–23.
72. Zhang S, Iyer S, Ran H, Dolgalev I, Wei W, Foster C, et al. Genetically defined, syngeneic organoid platform for developing combination therapies for ovarian cancer. bioRxiv 2020:2020.04.06.028597.
73. Zhang S, Dolgalev I, Zhang T, Ran H, Levine DA, Neel BG. Both fallopian tube and ovarian surface epithelium are cells-of-origin for high-grade serous ovarian carcinoma. Nat Commun 2019;10:5367.
74. Lanni JS, Jacks T. Characterization of the p53-dependent postmitotic checkpoint following spindle disruption. Mol Cell Biol 1998;18:1055–64.
75. Oplustil O'Connor L, Rulten SL, Cranston AN, Odedra R, Brown H, Jaspers JE, et al. The PARP inhibitor AZD2461 provides insights into the role of PARP3 inhibition for both synthetic lethality and tolerability with chemotherapy in preclinical models. Cancer Res 2016;76:6084–94.
76. Ianevski A, He L, Aittokallio T, Tang J. SynergyFinder: a web application for analyzing drug combination dose-response matrix data. Bioinformatics 2017;33:2413–5.
77. Dobin A, Davis CA, Schlesinger F, Drenkow J, Zaleski C, Jha S, et al. STAR: ultrafast universal RNA-seq aligner. Bioinformatics 2013;29:15–21.

78. Liao Y, Smyth GK, Shi W. featureCounts: an efficient general purpose program for assigning sequence reads to genomic features. Bioinformatics 2014;30:923–30.
79. Love MI, Huber W, Anders S. Moderated estimation of fold change and dispersion for RNA-seq data with DESeq2. Genome Biol 2014;15:550.
80. Buenrostro JD, Giresi PG, Zaba LC, Chang HY, Greenleaf WJ. Transposition of native chromatin for fast and sensitive epigenomic profiling of open chromatin, DNA-binding proteins and nucleosome position. Nat Methods 2013;10:1213–8.
81. Corces MR, Trevino AE, Hamilton EG, Greenside PG, Sinnott-Armstrong NA, Vesuna S, et al. An improved ATAC-seq protocol reduces background and enables interrogation of frozen tissues. Nat Methods 2017;14:959–62.